The stratospheric impact of the Chisholm PyroCumulonimbus eruption: Part I, nadir satellite perspective

M. Fromm[1], O. Torres[2], D. Diner[3], D. Lindsey[4], B. Vant Hull[5], R. Servranckx[6], E.P. Shettle[1], Z. Li[7]

1 Naval Research Laboratory, Washington D.C., USA
2 NASA-GSFC & UMBC-JCET, Greenbelt, MD, USA
3 Jet Propulsion Laboratory, Pasadena, CA, USA
4 NOAA/NESDIS/RAMMB, Fort Collins, CO, USA
5 NOAA/CREST, City College of New York, New York, USA
6 Canadian Meteorological Center, Dorval, Quebec, CA
7, Earth System Science Interdisciplinary Center, University of Maryland, College Park, MD, USA

Abstract

The pyrocumulonimbus storm near Chisholm, Alberta on 28 May 2001 has been studied in depth. However the impact of this eruption on the lower stratosphere has not been quantified. Here and in a companion paper we explore this question. This paper focuses on the "young" Chisholm smoke plume, from the age of ~3 hr to 1 week, as observed by quasi-nadir-viewing satellite instruments. GOES visible and infrared image loops reveal the pyroconvective lifecycle and initial transport of the smoke cloud. MISR stereographic heights are the first of their kind for a stratospheric cloud, showing smoke up to 5 km above the tropopause on 29 May. MODIS IR and visible images are analyzed to give constraints on plume height, optical thickness, and particle size. Infrared brightness temperature analyses reveal unique aspects of the "day after" Chisholm plume. Particle size is roughly an order of magnitude smaller than normal cirrus crystals. The daytime 29 May plume is optically thick at tropopause temperatures yet smoky brown. A transition from deep anvil blow off to "dry" smoke is still occurring after ~1.5 days.

TOMS aerosol index is used as a proxy for areas of particularly high smoke-plume altitude. The Chisholm smoke in the upper troposphere and lower stratosphere is traced with AI for one week as the plume blows across North America to western Europe. First estimates are made of stratospheric smoke-mass in relation to emissions during pyroconvection. The 29 May stratospheric Chisholm pyroCb plume contains a mass of ~1.94x10^4t, which represents between ~22% of particle emissions from this fire. This also represents ~5% of background northern hemispheric stratospheric sulfate aerosol mass.

1 Introduction

Smoke and other biomass burning emissions in the lower stratosphere (LS) have been observed and documented on at least nine occasions, in 1950 [*Penndorf*, 1953], 1992 [*Livesey et al.*, 2004], 1994 [*Waibel et al.*, 1999], two events in 1998 [*Fromm et al.*, 2000 and 2005; *Siebert et al.*, 2000], 2001 [*Fromm and Servranckx*, 2003, hereafter shown as FS03], 2002 [*Jost et al.*, 2004], 2003 [*Fromm et al.*, 2006], and 2004 [*Damoah et al.*, 2006]. In all except the earliest case the cause was either identified as or speculated to be large forest or bush fires involving deep pyroconvection. (The source in the Penndorf case was a large Canadian forest fire but convection was not identified or suspected.) The most extreme manifestation of pyrocumulus, now being called pyrocumulonimbus (pyroCb for short), is a fire-aided or -caused severe convective storm that reaches the upper troposphere, lower stratosphere (UTLS), involves lightning, precipitation and/or hail, extreme winds, and in some cases even tornadoes [*Fromm et al.*, 2006]. The role and importance of intense pyroCb in transporting smoke and other biomass burning emissions into the UTLS are still in the early stages of our understanding. Presently, the various aspects of this phenomenon are still incompletely characterized, but new observations, surveys, and simulations of the pyroCb are on the increase.

It has been established that pyroCb can produce a two to fivefold increase in zonal average lowermost stratospheric aerosol optical depth [*Fromm et al.* 2000, 2005, 2006].

Certain aspects of the pyroCb combustion/convection dynamic that enable the production and transport of such aerosol abundances into the LS are now being explored. For instance, the *Fromm et al.* [2006] case study of a pyroCb in Canberra Australia--aided by radar, photographs, and photogrammetric ground-damage assessment--found that the firestorm manifested unique cloud microphysics, spawned a tornado, and had plume characteristics consistent with a volcanic eruption [*Tupper et al.*, 2005]. Another case for which the details are being intensely studied is the Chisholm fire (Alberta Canada, 55°N, 114°W) and pyroCb of 28 May 2001 [FS03]. Several additional investigations of the Chisholm pyroCb have since been initiated because of the wealth of untapped data [e.g. *Rosenfeld et al.*, 2007, hereafter cited as R07] and a motivation to simulate the Chisholm pyroconvection [*Trentmann et al.*, 2006 and *Luderer et al.*, 2006] and smoke plume heating/lofting [*Stenchikov et al.*, 2006].

One area of uncertainty regarding extreme pyroconvection is the immediate post-convection plume. A quantitative understanding of the pyroCb injection is necessary for characterizing the eruption energetics, fuel consumption, and reconciling this "initial condition" of a UTLS plume with downstream impact. Works such as FS03 and *Fromm et al.* [2005] documented peculiar and suggestive qualities of the "day after pyroCb" plume observed from satellite. In summary, what was seen is a mesoscale cloud that is gray or smoky in color, opaque in the thermal infrared (LWIR) at brightness temperature (BT) representative of the tropopause region, and having an ultraviolet backscattering aerosol index (AI) of extremely large positive values [*Fromm et al.*, 2005]. In this paper we explore in detail the Chisholm pyroCb "day after" plume and the evolution of this plume in the week after the injection into the LS. The present work is motivated by revelations since FS03 that provide objective constraints on qualities such as the young plume's altitude. Moreover, the Total Ozone Mapping Spectrometer (TOMS) retrieval algorithm graduated to version 8 [*Bhartia*, 2007] since FS03, resulting in enhanced sensitivity of the AI to UTLS aerosols. This is a companion paper to *Fromm et al.*, [submitted 2007], which deals with profile views of the Chisholm plume as it evolved in the spring/summer of 2001.

In this work we integrate several available nadir and quasi-nadir satellite imager views of the Chisholm UTLS smoke plume in the first week after the pyroCb. The primary aim is to establish quantitative constraints on the young plume's UTLS altitude, geometric thickness, smoke-particle abundance and size. A second aim is to characterize the physical evolution of the plume in the first week after the injection. The satellite instruments consist of the Moderate Resolution Imaging Spectrometer (MODIS) [*King et al.* 1992; *Kaufmann et al.* 1997] and Multi-angle Imaging SpectroRadiometer (MISR) [*Diner et al.* 1998] aboard the Terra platform, Earth Probe TOMS [*Torres et a*l. 2002], and the Geostationary Operational Environmental Satellite (GOES).

In section 2 we describe the data sets used. Section 3 contains an analysis of the "day after" Chisholm plume as observed by GOES, TOMS, MODIS, and MISR. In Section 4 we compare MODIS and TOMS views of the Chisholm plume on 30 May 2001 with the 29 May "day after" plume. Section 5 contains the analysis of the movement of the plume in its first week revealed by TOMS AI maps. Discussion and summary are contained in Section 6.

2.0 Data Sets

2.1 MISR

MISR provides continuous multi-angle imagery of the sunlit Earth. The instrument contains nine charge-coupled-device-based pushbroom cameras to observe the Earth at nine discrete view angles: One view points toward nadir, and the other eight are symmetrical views at 26º, 46º, 60º, and 70° forward and backward of nadir. Images at each angle are obtained in four spectral bands centered at 446, 558, 672, and 866 nm. The swath width of the MISR imaging data is 400 km. It takes 7 minutes for any particular scene to be observed at all nine viewing angles. In its global observing mode, data from the red band of all of MISR's off-nadir cameras, and in the four bands of the nadir camera, are acquired at 275-m spatial resolution; all other channels are averaged on-board to 1.1-km resolution to conserve data rate. See *Diner et al.* [1998] for more details.

Ground data processing maps MISR radiances to a Space Oblique Mercator projection, which geolocates and co-registers the data from all instrument channels to both the WGS84 ellipsoid and to the surface terrain altitude. Geolocation uncertainty is estimated to be ±50 m, and co-registration errors are < 1 pixel (275 m). Ongoing assessments of image geolocation and co-registration are performed to ensure product quality [*Jovanovic et al.*, 2002, 2007]. The high resolution, ellipsoid-projected red-band radiances are operationally used in an automated algorithm to derive cloud-top and aerosol plume-top heights relative to the surface. Pattern matching is used to determine the geometric parallax (horizontal displacement) for elevated atmospheric features, and stereo-photogrammetric algorithms transform these parallaxes into cloud-top or plume-top heights [*Moroney et al.* 2002; *Muller et al.* 2002; *Zong et al.* 2002]. In the standard MISR Level 2 Stereo Product, which uses the nadir and 26º cameras in the height retrievals, the quantized precision of the resulting height field is ±560 m. Altitudes for clouds as well as smoke and dust plumes are routinely retrieved and reported on a 1.1-km resolution geolocated grid. Because the heights are derived geometrically, they are insensitive to atmospheric temperature profile, emissivity, and radiometric calibration uncertainties. Validation using ground-based 35/94 GHz radar and lidar retrievals of single-layer clouds shows instantaneous accuracies typically in the 500 m – 1 km range [*Naud et al.*, 2002, 2004, 2005a,b; *Marchand et al.*, 2007]. Since the technique is purely geometric, comparable accuracy is expected for aerosol layers.

Owing to the 7-minute interval from when MISR first sees a scene with the forward 70º camera to its last view with the backward 70º camera, the motion of clouds or aerosols during this time contributes to the disparity between image pairs and therefore must be distinguished from the parallax due to height. Consequently, a "wind correction" should in general be applied to the derived stereoscopic heights. This can be derived from a triplet of views (nadir, 46º, and 70º) [*Horváth, and Davies*, 2001; *Zong et al.*, 2002]. Only the along-track component of motion contributes to the uncorrected parallax error. The magnitudes of wind corrections are typically < 1 km in height. Given the better density of coverage typically obtained with the non-wind-corrected heights, and the generally small

height error associated with winds, it is often more convenient to ignore the wind corrections when the resulting uncertainty is tolerable.

Many aerosol plumes are too tenuous to be reliably detected in the nadir and 26º views which are used in MISR's operational height retrievals. However, the MISR 60º and 70º views are much more sensitive to thin plumes due to the oblique slant path. Specialized runs of the MISR stereo retrieval algorithm demonstrate that it works well with the oblique cameras and improves the height coverage for thin clouds, elevated aerosol layers, and near-surface plumes that the operational product currently misses.

2.2 TOMS Aerosol Index

The TOMS sensor detects UV absorbing aerosols with the well known AI parameter [*Herman et al,* 1997]. The AI is a measure of the spectral contrast change in the UV (331 and 360 nm) resulting from the presence in the atmosphere of light absorbing particles. Thus, the AI is primarily a measure of the 'missing' Rayleigh-scattered (and cloud-reflected) radiation at the top of the atmosphere that has been absorbed by the aerosols. The AI magnitude depends strongly on the aerosol layer height above the ground and its optical depth [*Torres et al.*, 1998]. The sensitivity of AI to aerosol layer height can be advantageously used for the unambiguous detection of UTLS absorbing aerosol layers generated by pyro-convection. These highly elevated aerosol layers yield unusually high AI values (10 or larger) clearly associated with their UTLS location. Aerosol Index values for large trospospheric aerosol loads associated with biomass burning of desert dust aerosols are typically no larger than about 8. The ability to detect UTLS absorbing aerosols is a clear improvement of the TOMS version 8 data [*Bhartia*, 2007]. In version 7 the AI data was artificially truncated at a value of 12.8. By removing this arbitrary limit the TOMS aerosol data has become a very useful tool for the detection and tracking of pyro-convection activity [*Fromm et al*., 2005].

2.3 MODIS

We use Terra MODIS collection 5 level 1b data [*Yang et al.* 2007 and references therein]. Our analysis uses 1 km resolution data from visible channels 1, 3, and 4 for true-color imagery, radiance data from the MWIR (3.92 μm) channel 22, and LWIR channels (11 and 12 μm) 31 and 32, all expressed as brightness temperature. The MODIS cloud algorithm is discussed by *King et al.* [1992 and 2003].

3.0 The Chisholm "day after" Smoke Plume: 29 May 2001

The Chisholm fire erupted into pyroconvection in late afternoon on 28 May 2001, at approximately 00 UTC 29 May (FS03). The active convection persisted for about three hours and created an opaque smoke/ice anvil with 11 μm brightness temperatures lower than -60°C, ~2°C lower than the tropopause temperature (R07). After 03 UTC the pyroconvection ceased and the residual plume, spanning the tropopause into the lowermost stratosphere, moved north toward the Northwest Territories (NWT). The evolution from pre-pyroCb to residual plume was captured with a day-long animation of GOES visible (during daylight) and midwave IR (MWIR) during nighttime for the period 22 UTC 28 May to 2345 UTC 29 May (see auxiliary material, S1). Here the visible frames are overlain with MWIR hot-spot pixels. The animation shows the apparently expanding/heating Chisholm fire, the pyroCb pulsing in two main phases, and the expansive cold/opaque cloud persisting through the night, After sunrise on 29 May the plume is a large, smooth gray cloud that spreads and arcs through NWT and then southeastward toward Hudson Bay. Next we will analyze the post-pyroCb plume with polar-orbiting satellite views at two times during this "day after."

3.1 Nighttime MODIS Views

Here we introduce MODIS MWIR and LWIR image data to gain insights into the Chisholm plume's height, opacity, and plume-particle size. The wealth of IR channels provided by MODIS is great; here we focus on wavelengths and techniques that have been successfully used on clouds and volcanic plumes. The chosen MWIR and LWIR channels are common among the operational geostationary and polar orbiting imagers.

Because some operational instruments do not employ a MWIR channel at ~3.9 μm, and because this MWIR sensor responds very differently at night vs. daytime (due to reflected sunlight during the day), we introduce a LWIR BT-difference technique that applies consistently in darkness and daylight.

The 29 May Terra MODIS nighttime IR imagery (0510 UTC, 2210 LST) captures the young plume about 3 hours after pyroconvection collapsed. Figure 1a gives the LWIR BT, which reveals that the Chisholm plume has a substantial area colder than -60°C. As R07 reported, this represents an optically opaque surface above the local tropopause. It is obvious from the low BT that the young Chisholm pyroCb plume is distinctive from all the other clouds in this scene, even though deep nonpyro-convection occurred the prior evening R07.

Figure 1b gives the 0510 UTC MODIS MWIR BT. During the day, satellite-detected radiation at this wavelength has both reflected solar and emitted terrestrial components [*Levizzani and Setvak*, 1996]. Here in darkness the MWIR BT pattern closely mimics that of 11 μm. In section 3.2.4 we contrast this with the daytime view.

3.1.1 THIR Brightness Temperature Difference (BTD)

Figure 1c contains a brightness-temperature difference image, the difference being between the 11 and 12 μm BT. This so-called "split-window" technique has been used to evaluate volcanic cloud composition [e.g. *Wen and Rose*, 1994] and meteorological cloud-particle size [*Gothe and Grassl*, 1993]. Split-window BTD is expected to be zero to slightly positive (i.e. generally < +1.0 K) for optically thick water-ice clouds. However, for high-altitude optically thin meteorological or volcanic cloud, BTD departs considerably from zero. Thin water-ice clouds over a warmer surface typically give a positive BTD [*Yamanouchi et al*., 1987]; ash-rich optically thin volcanic clouds may have the reverse effect, leading to negative BTD [*Prata*, 1989]. BTD has been used effectively as a detection method for yet another peculiar cloud form, the ice-rich high-

tropospheric volcanic plume [e.g. *Rose et al.*, 1995 and 2003]. The implication in such cases is that large positive BTD signifies anomalously small ice crystals populating a plume dominated by ice and ice-coated ash. In the present case of the 0510 UTC Chisholm pyroCb blowoff, BTD is near zero in the innermost portions of both residual anvils (where LWIR BT is quite cold), and strongly positive on the perimeter, especially the eastward side. In this zone the cloud edge overlies cloudless skies (note the adjacent "warm" LWIR BT in Figure 1a). The BTD here approaches +10°C, much larger than anywhere else in the MODIS scene.

According to the radiative transfer modeling schema of Figure 4a in *Guo et al*. [2004], BTD in this range is reserved for a population of cloud particles with exceptionally small effective radius compared to typical cirrus ice crystals. *Prata and Barton* [1993] used both a radiative transfer model and satellite LWIR observations to demonstrate the relation of BTD to 11μm BT for a range of cloud optical depth and ice crystal effective radius. Figure 6 therein shows that BTD is near zero for clear sky (warm LWIR) and optically thick, cold ice clouds, and increasingly positive in between. The positive departure from zero at a given optical depth or BT increases with decreasing particle size. Maximum BTD for cirrus cloud with nominal effective radius (~30 μm) is ~+3K in simulation and observation (their Figure 14).

We replicate that type of analysis with the 0510 UT MODIS data in Figure 2, BTD as a function of 11μm BT. The two scenes containing the pixels shown in Figure 2 are centered on the Chisholm plume (Figure 2a) and meteorological cloud (Figure 2b). Two densest clusters of pixels in Figure 2a are for clear-sky (warm BT) and deep, optically thick (cold) cloud. Like the simulation and observations of *Prata and Barton* [1993], the BTD at these limits is between 0 and 1K. The otherwise most obvious feature in Figure 2 is the arcing BTD in between these limits, reaching a maximum of ~+10K. A significant number of pixels exhibit both a very low BT and large positive BTD. Another dense clump of pixels is situated along the BTD~0K line between the coldest and warmest BT. Not shown, but determined in subsetting these data, this cluster came from the deep meteorological cloud west of the smoke plume; the pixels in the arc and those with

generally large BTD were in the periphery of the Chisholm plume. The high arc of BTD is consistent with particle effective radius of ~4-6 μm in the plume (much smaller than a nominal cirrus crystal of ~30 μm), according to *Prata and Barton*'s [1993] Figure 6. Figure 2b contains only meteorological cloud. Here the BTD is consistently low for all BT, with some spread in the midrange, a very different signature than the smoke plume's.

This analysis will be applied again for the daytime 29 May MODIS view of the Chisholm plume, discussed next. However, here we refer the reader to the auxiliary material section for a BTD analysis of the active pyroconvective phase of the Chisholm fire discussed in great detail by R07. The BTD pattern and distinction discussed above is observed to be quite consistent with the post-convection plume.

3.2 Daytime 29 May Views

3.2.1 MODIS Visible

Daytime (1840 UTC; 1140 LST) 29 May Terra MODIS views of the "day after" Chisholm plume are shown in Figure 3. A stretched true-color rendering in Figure 3a illustrates the breadth and abundance of smoke. Along the west, north, and east perimeter the smoke overlies pure white water ice cloud, with weak yet discernable shadowing suggesting higher smoke altitude. To the south a tongue of smoke is translucent over cloud-free sky. The perimeter smoke is relatively gray and smooth, and becomes dark brown and textured toward the core.

3.2.2 MODIS LWIR

Figure 3b shows the LWIR image. Much of the smoke plume core is opaque at BT < -40°C, which is a proxy for upper tropospheric altitude and represents a condition assuring homogeneous freezing [*Wallace and Hobbs*, 1977]. Thus any conventional cloud particles inside this contour would be in the form of ice. We see by comparison with the nighttime view in Figure 1a that the general cloud-top BT has increased but is still quite

low within the smoke plume —and lower than anywhere else in the image. Considering the spatial correspondence of low BT and smoky color—and the likelihood that this correspondence also applied during the overnight observation—we conclude from this plume-top "warming" that an evolutionary drying out of the smoke plume is taking place. I.e. smoke-polluted ice is sublimating, thereby transitioning to smaller crystals and "dry" smoke. It is worth noting again that the Chisholm plume's BT is still distinctively low compared with other clouds in this scene, and that there is no clear evidence of other convective blow off from the prior evening's "regular" convection. Hence the smoke-ice pyroCb plume appears to be a particularly persistent form of anvil blow off compared with "regular" Cb blow off.

3.2.3 MODIS BTD

The BTD at 1840 UTC is shown in Figure 3c. Here again the Chisholm plume has a distinctive signature—generally large BTD—albeit transformed from the nighttime view ½ day earlier. Here the area generally consisting of the smoky color (Figure 3a) is notably positive in BTD, however the maximum BTD is depressed in comparison to the nighttime view.

A BTD versus BT analysis like that of section 3.1.3 and supplemental data are shown in Figures 4 and 5. Figure 4 gives the true color and LWIR images with boxes showing where the BTD analysis is performed. We chose an exclusively meteorological cloud subscene (A), the plume and surrounding cloudy/clear area (B), and the core of the cold smoke plume (C). The BTD for A (Figure 5) is uniformly close to zero, from clear-sky through thick/cold cloud BT. For guidance and comparison, the vertical bar at BT~-40° is placed to isolate the coldest cloud tops. In addition, a wedge encasing the preponderance of pixels at BT < -40°C is drawn, and replicated on Figure 5b. We see that although nowhere is the plume BTD as large as at 0510 UTC, it is systematically greater than for the meteorological clouds, even in the inner core of the plume.

To our knowledge this peculiar set of conditions is not documented in the literature. This condition indicates that the plume-top composition and/or prevailing particle size is unique, a conclusion reinforced by the strong smoky coloration. Thus it appears that deep, optically thick "day after" pyroCb plumes can create a uniquely positive BTD signature. It would be valuable in future work to study other similar plumes from both an observational and radiative transfer modeling standpoint.

3.2.4 MODIS MWIR

Figure 3d gives the MWIR BT of the Chisholm plume and surrounding scene. Here we see significantly greater BT in the coldest part (ref. Figure 3b) of the plume, as compared with the nighttime MWIR and daytime LWIR. The plume's "warm" MWIR BT is primarily a consequence of increased reflectance associated with small cloud/smoke particles comprising the plume. This high-MWIR-reflectivity/small-cloud-particle relation has been exploited by several investigators (e.g. *Arking and Childs* [1985] and *Rosenfeld and Lensky* [1998]). The "warm" MWIR suggests that the "day after" Chisholm plume is comprised of a sufficient abundance of particles large (and concentrated) enough to create a deep, optically thick LWIR surface yet substantially smaller than a "normal" thick cirrus cloud. Our interpretation of the BTD analysis reinforces the idea that the plume-particle effective size is strongly suppressed in comparison to typical cirrus crystals. This convoluted plume probably represents a transitional mode which—roughly 17 hours after pyroconvection--consists of "dry" smoke particles, a size spectrum of evaporating smoky ice crystals, and pure water-ice cloud crystals. However, it is important to note that the brown color of the plume means that the dominant material at the cloud top is smoke.

The Chisholm plume's MWIR pattern in Figure 3d has a notable feature--localized areas wherein the BT is quite low. The color scale we chose shows these areas as green patches. These are mostly found near the northern perimeter of the smoke plume, where according to the visible and LWIR images it is apparent that the smoke plume is higher than the other clouds--colder and casting a shadow on the water-ice cloud deck. In this

nearly noon local time frame, the solar azimuth is essentially southerly so the shadows are cast preferentially northward. In shadows, the MWIR BT will behave similarly to nighttime scenes, during which the MWIR and LWIR BT are in closer agreement. We take advantage of this clue in another portion of the Chisholm plume, pointed out by the arrow in Figure 3d. Here in the southwestern plume segment, where the color of the surface is deep brown, the MWIR BT is relatively cold (green). Since this part of the plume is obviously smoky, the most logical reason for the low MWIR BT is shadowing. We examined a zoomed, high-resolution true-color image of this area (not shown) and confirm an apparent higher deck of smoky material southwest of the "cold" MWIR BT, casting a perceptible shadow. Thus the general smoky canopy in visible view of Figure 3a has subtle layer textures revealed by the MWIR image. This will have implications on the analysis of the plume height discussed next.

3.2.5 MISR

The eastern portion of the Chisholm plume sampled by MODIS was simultaneously sampled by MISR also on the Terra satellite (Figure 6). The natural color view is from the MISR 60° forward viewing camera. A pall of yellowish smoke is apparent both above the surface and clouds. The smoke appears thicker at the oblique view angle, thus better areal coverage is obtained and the height retrievals are less sensitive to the underlying cloud deck. The right-side panel is a specially-generated stereo height product using MISR's 46° and 60° forward-pointing cameras. The southern portion of the smoke cloud is at an altitude of about 3.5 km; however, the smoke further to the north is at heights of about 12-13 km asl. The height fields pictured here are uncorrected for wind effects; wind-corrected heights (which have higher accuracy but sparser spatial coverage) for this smoke pall are about 0.5 km higher.

Figure 7 shows a "profile" of MISR stereo height from the scene in Figure 6. This is simply a frequency distribution of the heights, and we focus on the local maxima. From these we conclude that there are primarily three cloud or plume decks in the MISR scene. By sub-setting the stereo height image we can identify the distinct compositions to the

three decks. The lowest deck, at ~3.2 km ASL, is the tongue of smoke in the southern portion of the MISR scene. The water-ice cloud deck is mostly between 6.5 and 8.0 km. The high smoke is grouped at 12.0 km, 2-3 km above the tropopause, which here is determined from the 12 UTC 29 May radiosonde from Fort Smith, NWT (not shown). The MISR stereo height retrievals of the "day-after" Chisholm plume are the first independent, objective assessments of the initial stratospheric injection potential of a pyroCb.

3.2.6 TOMS AI

Next we introduce level 2 TOMS AI (Figure 8). Each pixel is mapped at its effective resolution taking into account the TOMS scan pattern. The time of these measurements is ~18 UTC, about 0.75 hr earlier than the Terra overpass, thus sampling approximately the same scene as Terra. The peak AI is 31.2 in the core of the smoke plume, roughly where the MODIS color of the smoke is intense brown. In the version 7 result reported by FS03, the plume core AI had an artificial limit of 12.8, thus we see an immediate advantage to the version 8 AI retrieval. In our investigation of level 2 AI for other thick and deep smoke plumes (which includes published cases cited in Section 1 and several other works in progress), the peak value of 31.2 is unrivaled. Although the aerosol index is ultimately a qualitative indicator, the relevance of values in the 20s and 30s is evident in the context of the MODIS smoke color, low brightness temperature, and MISR stereo heights—they signify a plume with particularly high absorption optical depth and high altitude aerosols. Next we attempt to explore these relations more exhaustively.

3.3 Plume and Cloud Height

The combination of satellites viewing the 29 May Chisholm day-after plume allows us to glean greater insights into the cloud/plume complex. We choose 65°N for a slice through the core of the smoke. In Figures 9 and 10 we show MISR, MODIS, and TOMS data within ±2° latitude, from 125° to 95°W, which spans the smoke pall and continues through a solid deck of pure water-ice clouds to the east and west. In each figure we plot

individual pixel values and a solid line, a boxcar average chosen to discern a general pattern but preserve small-scale structure.

Figure 9 contains MISR stereo heights and TOMS AI, and an effective opaque cloud-top height derived from MODIS LWIR BT. Here we use a temperature profile from NCEP Reanalysis for 12 UTC 29 May interpolated to 65°N, 110°W for the BT-height relation. We see that the entire slice is comprised of cloud; i.e. BT gives an unbroken stretch of elevated heights, from 3.0 to 10.5 km. Cloud tops estimated in this way are near 5 km ASL at the east and west ends, and rise toward the center longitudes. To assess cloud altitude with respect to the tropopause, we determine the local tropopause region using two approaches. The top of the tropopause region is the altitude of the temperature minimum, averaged from the radiosonde profiles at Fort Smith (60ºN, 110ºW) and Cambridge Bay (69ºN, 105ºW) for each station's two 29 May measurements. This value is 11.1 km. The tropopause height is calculated by the dynamical definition, using potential vorticity equal to 2.5 potential vorticity units, for the 12 UT 29 May NCEP reanalysis fields. That gives a tropopause height at 65N, 110W of 10.5 km. The opaque cloud tops rise to the tropopause at 114°W. Both AI and BT-estimated cloud heights rise toward the center of this slice at 65°N. At the east and west edges, the AI is essentially zero, which means no absorbing aerosol above the surface observed by TOMS. The sharpest gradients of AI are where the MODIS BT-height gradients are also largest, between ~114°-116°W and 102°-105°W. In the plume-core longitudes, where the BT-height is greatest, the correlation with AI breaks down. The peak AI is at ~111°W, about 3° east of the deepest opaque cloud top. Considering the very strong aerosol signal in the MODIS color throughout the core of the plume, the peaking of AI at 111°W may well indicate a local maximum in plume altitude instead of an increase in optical depth. This decoupling of the correlation between LWIR BT and AI would occur if the smoke aerosols here were small enough to be transparent to emitted 11μm radiance. In summary the strong positive correlation between the AI and BT-height gradients approaching the plume core indicates that the plume-core AI variation reveals a local maximum in smoke altitude.

We can assess this independently with the MISR stereo heights. Even though the MISR swath does not cover the entire slice in Figure 9, these data offer a distinct advantage over MODIS LWIR BT, because the stereo height retrieval does not depend on LWIR opacity. Moreover, the MISR swath contains both meteorological cloud and smoke, and covers a portion of the AI swath where values range from marginal to extreme. We see that in the eastern edge of the MISR swath, where AI is ~3 (just above noise levels), the typical MISR stereo height (~5.7 km) is relatively close to the BT-height estimate (~5km). Here the dominant reflecting layer is the water-ice cloud deck. But the rapidly "thickening" smoke to the west gives MISR stereo heights that increase more rapidly than the MODIS BT-height estimate. Near the western edge of the MISR swath, where AI is over 20, the MISR-MODIS height difference is between 2-5 km. At the western edge the central values of MISR stereo height are above the tropopause and the east-to-west slope is still positive. Here the AI slope is also positive. Thus it appears that the smoke plume to the west of the MISR swath at 65°N continues to increase in height and is mainly in the lowermost stratosphere. It is not possible to resolve the relative contribution of increasing aerosol optical depth and plume altitude for the peaking of AI, but we attempt to address that by invoking MODIS visible data in Figure 10.

In Figure 10 we keep the MISR stereo heights and TOMS AI, but replace MODIS IR data with visible reflectance at the three wavelengths used in the true-color imagery. By plotting these, color coded accordingly, we can infer changes to optical depth by changes in color with respect to the general whiteness of the water-ice cloud deck that covers the west and east extrema of the slice at 65°N. The white water-ice cloud by definition gives approximately equal reflectances at the three true-color wavelengths. The brown hue of the smoke plume (see Figure 3a) is a result of relatively small reflectance contribution at the short (i.e. blue) wavelength, and dominance of red plus green wavelengths. Total brightness of the scene can be inferred by the "sum" of the three channels' reflectances. On the west and east edges of the scene in Figure 10, where the water-ice cloud deck dominates, the total visible reflectance is large while the red and green reflectances are equal to or even less than the blue-channel reflectance. Toward the center from each direction the blue-channel reflectance diminishes preferentially, first in a transition zone,

and bottoms out between 108.5 and 113W, where there is no discernable change in the intensity of the red+green versus blue reflectance. This may be viewed as a zone where the color-inferred aerosol abundance is both large and essentially unchanging. But it is within this zone that the smoothed AI line increases to a peak at 111°W. Considering our earlier interpretation of the increasing AI being strongly driven by plume altitude, this peaking of AI in the zone of thickest—and approximately constant--smoke aerosol suggests increasing plume altitude even above the high west-end MISR values.

Finally we come back to the point made in section 3.2.1 regarding smoke layers casting shadows and impacting MWIR BT. This particular feature is somewhat south of 65N, yet at a location where the color, AI, and LWIR BT are all near their most extreme values. Thus the apparent smoke layer discussed in 3.2.1 would be even locally higher than the heights we inferred in the discussion of Figures 9 and 10. It seems logical that in portions of the plume's core such as this, smoke reached an even higher altitude in the stratosphere.

3.4 Stratospheric Smoke Mass

We can estimate the mass of smoke injected into the lower stratosphere using inferences gained from the previous analysis. The synthesis of the AI with MODIS and MISR allows us to conclude that the parts of the Chisholm plume with AI greater than a certain threshold are above the tropopause. The analysis of Figures 9 and 10 allow us to suggest two thresholds: AI=15 and 19. The AI=19 threshold is taken as a conservative value—more likely to exclude stratospheric smoke than to include a false stratospheric measurement.

For the smoke-mass calculation we have performed a special retrieval of smoke optical properties using a radiative transfer model [*Torres et al.* 2005]. To permit a retrieval of extinction optical depth, the simulation fixes the plume effective altitude (based on the MISR stereo heights) at 12 km. The simulation then solves for optical depth and single scatter albedo in an iterative process. After convergence, values for optical depth are

available for each pixel. Although not shown, the extinction optical depth of the pixels with AI > 15 ranged between 0.321 and 0.723. We assumed a specific extinction-mass factor of 5 m^2/kg [*Reid et al.*, 2005]. Mass per pixel is then the product of the extinction optical depth, specific extinction, and pixel area.

Integrating the TOMS pixel footprint for the above-mentioned thresholds gives an area range of $1.17x10^5$ to $1.63x10^5 km^2$ (mean=$1.43x10^5 km^2$). The resultant mass of smoke is between $1.44x10^4$ and $1.94x10^4$t (mean=$1.69 x10^4$t). As a point of qualitative comparison, we relate this burden to the integrated northern hemispheric stratospheric aerosol burden for near background conditions (1979) calculated by *Kent and McCormick* [1984]: ~$3 x10^5$t. The Chisholm pyroCb injected an amount of smoke aerosol equivalent to approximately 5.6% of the background hemispheric aerosol load.

Now we reconcile the stratospheric smoke injection with emissions from the Chisholm fire during pyroconvection. Area burned during the blowup on 28 May was approximately 50000 ha [*Luderer et el.*, 2006 and references therein]. Total particulate matter emitted (TPM) from an area burned is expressed per equation (1)

TPM = Emission factor x Fuel load/area x Area burned (1).

Combusted fuel consists of surface and crown matter. For the area burned during the 28 May pyroconvection this is the sum of ~9.0 kg/m^2 for the surface [*ASRD*, 2001] and 1.0 kg/m^2 for the crown [*Brian J. Stocks*, personal communication, 2007]. For emission factor we take two values from Table 6 of *Reid et al*., [2005] for temperate/boreal forest, to give a range of emissions (expressed as the ratio of kg emitted to kg consumed): those of *Hobbs et al.* [1996] (.018) and *Nance et al.* [1993] (.029). These bracketing values result in total particulate emissions between $9.0x10^4$t and $1.45x10^5$t. The stratospheric smoke-mass injection from the Chisholm pyroCb was between 0.29% and 0.39% of fuel consumed during pyroconvection. In relation to TPM, the fraction of stratospheric smoke was between 10% and 22%. The simulation of the Chisholm pyroCb by *Trentmann et al*. [2006] resulted in a stratospheric aerosol injection proportion of 8%.

4.0 Comparison of 29 and 30 May Views

Figure 11 contains the MODIS daytime views of the Chisholm plume on 30 May (1745 UTC). At this time the plume stretches from NWT across Hudson Bay and into the Great Lakes and Michigan. According to the true color image in Figure 11a the smoke is evidently thinner than on 29 May and spread over a much greater horizontal footprint. Skies over adjacent land surfaces in Canada and US are apparently cloud free. Over Hudson Bay there appears to be widespread ice and some overlying water-ice cloud, detectable through the translucent smoke. The LWIR image of Figure 11b reinforces the idea that land areas of the upper Midwest US and Manitoba are cloud free. Northern and central Hudson Bay has opaque low and mid-tropospheric cloudiness. The smoke plume from James Bay to Lake Superior appears to have a residual signal in LWIR, indicating that the transition from opaque smoky ice to transparent smoke is not yet complete, ~1.5 days after pyroconvection.

TOMS AI map for 30 May is shown in Figure 12a. The times of the Terra and Earth-Probe overpasses coincide within two hours. Not surprisingly, the same general shape of the MODIS view of the plume is reproduced. However, the AI gives detail that allows us to infer local extrema in plume altitude. There are two local AI maxima. In both areas AI>20, values representative of the core of the 29 May plume. At neither AI maximum is the visible optical thickness apparently as large as it was on 29 May—thus the large AI probably indicates plume altitude extremes. One of the maxima is west of James Bay. Here the plume in the true-color MODIS view is obvious but portions of the plume south of the AI maximum and north of the Canada/US border are equally optically thick in the visible--and LWIR--but do not create an equal AI. Thus this and the other AI maximum to the north probably identify where the plume protrudes most deeply into the stratosphere. Moreover, this section of the plume's footprint lags far behind the downwind edge over Michigan. Considering the establishment that the core of the 29 May plume topped out well into the lower stratosphere—thus above jet stream altitude—it is reasonable to conclude that the young Chisholm smoke plume spanned the UTLS,

and as it deformed during advection the part at jet-stream level advanced far beyond (i.e. to Michigan on 30 May) the highest stratospheric smoke over and/or near Hudson Bay.

5.0 The Chisholm Plume's First Week

The evolution of the Chisholm smoke plume for the balance of its first week of existence is captured in the AI maps of Figure 12. As expected, the maximum AI on each day between 31 May and 4 June declines as the plume shears horizontally. The plume snakes into a wave signature on 31 May, crossing the US Atlantic coast and extending to Labrador. Note the reproduction of two localized AI maxima, one in "mid" plume and the other lagging over James Bay. On 1 June, as the plume takes on a complete wave signature between Quebec and just south of Iceland, a distinct AI maximum appears in the "trough" of the wave over the Atlantic near 38N (again lagging far behind the plume's leading edge). By 2 June the leading portion of the Chisholm smoke plume passes over the United Kingdom and resides as far eastward as France, while the western portion (including the AI maximum) starts to form into an apparent cyclonic shape over the central Atlantic. On 3 and 4 June the AI pattern breaks up; the downwind (i.e. eastern) edge enters the Mediterranean region while the lagging plume over the central Atlantic appears to swirl and stagnate. In general the persistence of an AI plume for one week and the distance between Alberta and the Mediterranean Sea is by itself an indicator of an extremely unusual aerosol perturbation. This perturbation consists of a large abundance of aerosol material and a residence altitude likely from upper tropospheric jet stream levels to several km into the lower stratosphere.

6.0 Summary

Our aim was to characterize and establish important parameters related to a young stratospheric smoke plume. The case chosen is that of the Chisholm (Alberta) pyroCb of 28 May 2001. This case, now the subject of multiple papers, is an excellent example of the most extreme form of pyroconvection because of the many space- and ground-based observations of the blowup and aftermath. We focused on the immediate aftermath (from

hours to 1 week old), which is an important timeframe for regional or global transport/chemistry/cloud-process models to consider as initial conditions.

The Chisholm pyroCb (FS03, R07) has now been confirmed to have injected a large quantity of smoke into the lower stratosphere, even above the altitude of the local temperature minimum, as evidenced from satellite imagery less than ½ day after the pyroconvection ended. MISR stereoscopic height retrievals give the first independent, objective, and detailed confirmation of stratospheric smoke in a young pyroCb plume. MODIS true-color and IR imagery, TOMS aerosol index and MISR stereo heights together allowed us to gain advanced insights into these peculiar UTLS pyroCb plumes. For instance, level 2 AI can reveal variations of plume altitude within a broad or optically thick plume.

The Chisholm pyroCb stratospheric plume on the day after injection covered an area of approximately1.43×10^5 km^2, with a mass estimated at between 1.44×10^4 and 1.94×10^4t. This represented between 10 and 22% of the total particulate emissions during pyroconvection, and about 0.3% of the total fuel consumed. It also was related to hemispheric sulfate aerosol background burden; estimated to be roughly 5.6% of hemispheric aerosol by mass.

Visible, MWIR BT and LWIR BTD analysis of the "day after" Chisholm plume led us to conclude that the uppermost particles in the young plume were a peculiar mixture of unadulterated dry smoke and smoky ice crystals significantly smaller than normal high cirrus ice crystals. The color of the plume and AI proved that the dominant material in the plume was smoke. This smoky cloud's core was effectively opaque in LWIR at the tropopause.

The Chisholm smoke plume "dried out" into transparent (in LWIR) smoke in a process that exceeded 1.6 days, a significantly longer sublimation time scale than for normal cumulonimbus cirrus blow off. AI of the aging Chisholm plume was used to locate the maximum stratospheric plume height, which lagged far behind the leading edge. After

one week the plume's leading edge had snaked as far east the central Mediterranean; a portion (perhaps the highest smoke) of the plume lagged, stagnated, and circulated over the mid-Atlantic. The companion paper by *Fromm et al.* [2007] presents initial profile measurements of the Chisholm plume there on 5 June and upstream over Quebec (near the tail end of the AI plume) on 1 June.

For the first time, several important initial constraints are placed on an extreme pyroCb event that polluted an entire hemisphere (see the companion paper, *Fromm et al.* [2007]). A single pyroconvective explosion has now been documented from the ground to the stratosphere with metrics that will enable comparisons with other pyroCbs, volcanoes, and conventional aerosol measures for the stratosphere.

Acknowledgements

We wish to thank Rong Rong Li for her assistance with the MODIS data. We are also grateful to Bill Rose for his expert insights with respect to the split window analysis. MDF and EPS were supported in part by a grant from the NASA Office of Earth Science and in part by NRL internal funding (from the Office of Naval Research). The views, opinions, and findings in this report are those of the authors, and should not be construed as an official NOAA and or U.S. Government position, policy, or decision.

References

Arking, A., and J. Childs (1985), Retrieval of Cloud Cover Parameters from Multispectral Satellite Images, *J. Clim. and Appl. Meteor*., 24, 322-333.

ASRD: Final Documentation Report (2001), Chisholm Fire (LWF-063), Forest Protection Division, ISBN 0-7785-1841-8, Tech. rep., Alberta Sustainable Resource Development.

Bhartia, P.K. (2007), Total Ozone from backscattered ultraviolet measurements, pp 48-63 in *Observing Systems for Atmospheric Composition*, G. Visconti, P. Di Carlo, W.H. Brune, M. Schoeberl, A. Wahner, editors, Springer.

Damoah, R., N. Spichtinger, R. Servranckx, M. Fromm, E. Eloranta, I. Razenkov, P. James, M. Shulski, C. Forster, and A. Stohl (2006), A case study of pyro-convection using transport model and remote sensing data, *Atmos. Chem. Phys.*, 6, 173-185.

Diner, D.J., J.C. Beckert, T.H. Reilly, C.J. Bruegge, J.E. Conel, R. Kahn, J.V. Martonchik, T.P. Ackerman, R. Davies, S.A.W. Gerstl, H.R. Gordon, J-P. Muller, R. Myneni, R.J. Sellers, B. Pinty, and M.M. Verstraete (1998), Multi-angle Imaging SpectroRadiometer (MISR) description and experiment overview. *IEEE Trans. Geosci. Rem. Sens.*, 36 (4), 1072-1087.

Fromm, M., J. Alfred, K. Hoppel, J. Hornstein, R. Bevilacqua, E. Shettle, R. Servranckx, Z. Li, and B. Stocks (2000), Observations of boreal forest fire smoke in the stratosphere by POAM III, SAGE II, and lidar in 1998, *Geophys. Res. Lett.*, *27*, 1407-1410.

Fromm, M., and R. Servranckx (2003), Transport of forest fire smoke above the tropopause by supercell convection, *Geophys. Res. Lett.*, *30* (10), 1542.

Fromm, M., R. Bevilacqua, R. Servranckx, J. Rosen, J.P. Thayer, J. Herman, and D. Larko (2005), Pyro-cumulonimbus injection of smoke to the stratosphere: observations and impact of a super blowup in northwestern Canada on 3-4 August 1998, *J. Geophys. Res.*, *110* (D8), D08205.

Fromm, M., A. Tupper, D. Rosenfeld, R. Servranckx, and R. McRae (2006), Violent pyro-convective storm devastates Australia's capital and pollutes the stratosphere *Geophys. Res. Lett.*, 33, L05815, doi:10.1029/2005GL025161.

Gothe, M. and H. Grassl (1993), Satellite remote sensing of the optical depth and mean crystal size of thin cirrus clouds and contrails, *Theor. Appl. Climatol.*, 48, 101-113.

Guo, S., W. Rose, G. Bluth, I. M. Watson (2004), Particles in the great Pinatubo volcanic cloud of June 1991: The role of ice, *Geochem. Geophys. Geosystems*, 5, 5, Q05003, doi:10.1029/2003GC000655.

Herman, J.R., P.K. Bhartia, O. Torres, C.Hsu , C. Seftor, and E. Celarier (1997), Global Distribution of UV-absorbing Aerosols From Nimbus-7/TOMS data*, J. Geophys. Res.*, 102, 16911-16922.

Hobbs, P., J. Reid, J. Herring, J. Nance, R. Weiss, J. Ross, D. Hegg, R. Ottmar, C. Liousse (1996), Particle and trace-gas measurements in smoke from prescribed burns of forest products in the Pacific Northwest, in: *Biomass Burning and Global C*hange, Vol. 1, edited by: Levine, J. S., 697-715, MIT Press, New York, 1006.

Horváth, Á. and R. Davies (2001), Simultaneous retrieval of cloud motion and height from polar-orbiter multiangle measurements. *Geophys. Res. Lett*. 28, 2915-2918.

Jost, H., K. Drdla, A. Stohl, L.Pfister, M. Loewenstein, J. Lopez, P. Hudson, D. Murphy, D. Cziczo, M. Fromm, T. Bui, J. Dean-Day, M. Mahoney, E. Richard, N. Spichtinger, J. Vellovic, E. Weinstock, J. Wilson, and S. Wofsy (2004), In-situ observations of mid-latitude forest fire plumes deep in the stratosphere, *Geophys. Res. Lett.*, *31*, L11101, doi:10.1029/2003GL019253.

Jovanovic, V.M., M.A. Bull, M.M. Smyth, and J. Zong (2002), MISR in-flight camera geometric model calibration and georectification performance. *IEEE Trans. Geosci. Remote Sens.* 40, 1512-1519.

Jovanovic, J., C. Moroney, and D. Nelson (2007), Multiangle geometric processing for globally geo-located and co-registered MISR image data. *Rem. Sens. Environ*., 107, 22-32.

Kaufman, Y. J., D. Tanré, L. A. Remer, E. F. Vermote, A. Chu, and B. N. Holben (1997), Operational remote sensing of tropospheric aerosol over land from EOS moderate resolution imaging spectroradiometer. *J. Geophys. Res.*, 102, 17051-17068.

Kent, G., and M. McCormick (1984), SAGE and SAM II measurements of global stratospheric aerosol optical depth and mass loading, *J. Geophys. Res*., 89, D4, 5303-5314.

King, M. D., Y. J. Kaufman, W. P. Menzel, and D. Tanré (1992), Remote sensing of cloud, aerosol, and water vapor properties from the Moderate Resolution Imaging Spectrometer (MODIS). *IEEE Trans. Geosci. Remote Sens.*, 30, 1-27.

King, M. D., W. P. Menzel, Y. J. Kaufman, D. Tanré, B. C. Gao, S. Platnick, S. A. Ackerman, L. A. Remer, R. Pincus, and P. A. Hubanks (2003), Cloud and aerosol properties, precipitable water, and profiles of temperature and humidity from MODIS. *IEEE Trans. Geosci. Remote Sens.*, 41, 442-458.

Levizzani, V. and M. Setvak (1996), Multispectral, high resolution satellite observations of plumes on top of convective storms, *J. Atmos, Sci*., 53, 361-369.

Livesey, N., M. Fromm, J. Waters, G. Manney, M. Santee, and W. Read (2004), Enhancements in lower stratospheric CH3CN observed by UARS MLS following boreal forest fires, *J. Geophys. Res.*, *109* (D06308), doi:10.1029/2003JD004055.

Luderer, G., J. Trentmann, T. Winterrath, C. Textor, M. Herzog, H. F. Graf, M. O. Andreae (2006), Modeling of biomass smoke injection into the lower stratosphere by a large forest fire (Part II): sensitivity studies, *Atmos. Chem. Phys.*, 6, 5261-5277.

Marchand, R.T., T.P. Ackerman, and C. Moroney (2007), An assessment of Multi-angle Imaging SpectroRadiometer (MISR) stereo-derived cloud top heights and cloud top winds using ground-based radar, lidar and microwave radiometers. *J. Geophys. Res*., in press.

Moroney, C., R. Davies, and J-P. Muller (2002), Operational retrieval of cloud-top heights using MISR data. *IEEE Trans. Geosci. Remote Sens.* 40, 15-41.

Muller, J-P., A. Mandanayake, C. Moroney, R. Davies, D.J. Diner, and S. Paradise (2002), MISR stereoscopic image matchers: Techniques and results. *IEEE Trans. Geosci. Remote Sens.* 40, 1547-1559.

Nance, J., P. Hobbs, L. Radke, D. Ward (1993), Airborne measurements of gases and particles from an Alaskan wildfire, *J. Geophys. Res*., 98, 14873-14882.

Naud, C., J.-P. Muller, and E. E. Clothiaux (2002), Comparison of cloud top heights derived from MISR stereo and MODIS CO2-slicing, *Geophys. Res. Lett.,* 29, Art. No. 1795.

Naud C., J.-P. Muller, M. Haeffelin, Y. Morille, and A. Delaval (2004), Assessment of MISR and MODIS cloud top heights through inter-comparison with a back-scattering lidar at SIRTA, *Geophys. Res. Lett.,* 31, L04114.

Naud, C. M., J. P. Muller, E. C. Slack, C. L. Wrench, and E. E Clothiaux (2005a), Assessment of the performance of the Chilbolton 3-GHz advanced meteorological radar for cloud-top-height retrieval, *J. App. Meteor*., 44, 866-877.

Naud, C. M., J.-P. Muller, E. E. Clothiaux, B. A. Baum, and W. P. Menzel (2005b), Intercomparison of multiple years of MODIS, MISR and radar cloud-top heights. *Annales Geophysicae*, 23, 1–10.

Penndorf, R. (1953), *On the phenomenon of the colored sun, especially the "blue" sun of September 1950*, AFCRC Technical Report 53-7, Air Force Cambridge Research Center, Cambridge, Massachusetts, 20, 41 pp.

Prata, A. J. (1989), Infared radiative transfer calculations for volcanic ash clouds, *Geophys. Res. Lett*., 16, 11, 1293-1296.

Prata, A. J. and I. J. Barton (1993), A multichannel, multiangle method for the determination of infrared optical depth of semitransparent high cloud from an orbing satellite. Part I: Formulation and simulation, *J. Applied Meteor*., 32, 7, 1623-1637.

Reid, J., R. Koppmann, T. Eck, and D. Eleuterio (2005), A review of biomass burning emissions part II: intensive physical properties of biomass burning particles, *Atmos. Chem. Phys.*, 5, 799-825.

Rose, W., D. Delene, D. Schneider, G. Bluth, A. Krueger, I. Sprod, C. McKee, H. Davies and G. Ernst (1995), Ice in the 1994 Rabaul eruption cloud: implications for volcano hazard and atmospheric effects, *Nature*, 375, 477-479.

Rose, W., Y. Gu, I. Watson, T. Yu, G. Bluth, A. Prata, A. Krueger, N. Krotkov, S. Carn, M. Fromm, D. Hunton, G. Ernst, A. Viggiano, T. Miller, J. Ballentin, J. Reeves, J.

Wilson, B. Anderson D. Flittner (2003), The February-March 2000 eruption of Hekla, Iceland from a satellite perspective,*AGU Geophysical Monograph 139: Volcanism and the Earth's Atmosphere, ed by A Robock and C Oppenheimer, pp. 107-132,* ISBN 0-87590-998-1.

Rosenfeld, D., and I. Lensky (1998), Spaceborne sensed insights into precipitation formation processes in continental and maritime clouds, *The Bulletin of American Meteorological Society*, *79*, 2457-2476.

Rosenfeld, D., M. Fromm, J. Trentmann, G. Luderer, M. Andreae, R. Servranckx (2007), The Chisholm firestorm: observed microstructure, precipitation, and lightning activity of a pyro-cumulonimbus, *Atmos. Chem. Phys.*, 7, 645-659.

Siebert, J., C. Timmis, G. Vaughan, and K. Fricke (2000), A strange cloud in the Arctic summer 1998 above Esrange (68N), Sweden, *Annales Geophysicae*, 18, 505-509.

Stenchikov, G., M. Fromm, E. Shettle (2006), Study of long-range transport and stratosphere-troposphere exchange in smoke plumes from forest fires caused by aerosol solar heating", *Eos Trans. AGU, 87*(52), Fall Meet. Suppl., Abstract A43A-0114.

Torres, O., P. K. Bhartia, J. R. Herman, Z. Ahmad, J. Gleason (1998), Derivation of aerosol properties from satellite measurements of backscattered ultraviolet radiation: Theoretical basis, J. Geophys. Res., 103(D18), 23321-23322, 10.1029/98JD02709.

Torres O., P.K. Bhartia, J.R. Herman and Z. Ahmad (2002), Derivation of aerosol properties from satellite measurements of backscattered ultraviolet radiation. Theoretical Basis, *J. Geophys. Res.*, 103, 17099-17110, 1998.Torres, O., P.K. Bhartia, J.R. Herman, A. Sinyuk, P. Ginoux, and B. Holben, A Long-term record of aerosol optical depth from TOMS observations and comparison to AERONET measurements, *J. Atmos. Sci.*, 59(3), 398-413.

Torres, O., P. K. Bhartia, A. Syniuk, and E. Welton (2005),TOMS Measurements of Aerosol Absorption from Space: Comparison to SAFARI 2000 Ground-based Observations, *J. Geophys. Res.*, 110, D10S18, doi:10.1029/2004JD004611

Trentmann, J., G. Luderer, T. Winterrath, M. D. Fromm, R. Servranckx, C. Textor, M. Herzog, H.-F. Graf, M. O. Andreae (2006), Modeling of biomass smoke injection

into the lower stratosphere by a large forest fire (Part I): reference simulation, *Atmos. Chem. Phys.*, 6, 5247-5260.

Tupper A., J. S. Oswalt, D. Rosenfeld (2005), Satellite and radar analysis of the volcanic-cumulonimbi at Mount Pinatubo, Philippines, 1991, J. Geophys. Res., 110, D09204, doi:10.1029/2004JD005499.

Waibel, A.E., H. Fischer, F.G. Wienhold, P.C. Siegmund, B. Lee, J. Ström, J. Lelieveld, and P.J. Crutzen (1999), Highly elevated carbon monoxide concentrations in the upper troposphere and lowermost stratosphere at northern midlatitudes during the STREAM II summer campaign in 1994, *Chemosphere: Global Change Science*, 1, 233-248.

Wallace, J. and P. Hobbs (1977), *Atmospheric Science: An Introductory Survey*, Academic Press, ISBN 0-12-732950-1.

Wen, S. and W. Rose (1994), Retrieval of sizes and total masses of particles in volcanic clouds using AVHRR bands 4 and 5, *J.Geophys. Res.*, 99, 5421-5431.

Yamanouchi, T., K. Suzuki, and S. Kawaguchi (1987), Detection of clouds in Antarctica from infrared multispectral data of AVHRR, *J. Meteorol. Soc*., 65, 949-961.

Yang, P., L. Zhang, G. Hong, S. L. Nasiri, B. A. Baum, H. L. Huang, M. D. King, and S. Platnick (2007), Differences between collection 4 and 5 MODIS ice cloud optical/microphysical products and their impact on radiative forcing simulations. *IEEE Trans. Geosci. Remote Sens.* (In Press).

Zong, J., R. Davies, J-P. Muller, and D.J. Diner (2002), Photogrammetric retrieval of cloud advection and top height from the Multi-angle Imaging SpectroRadiometer (MISR). *Photogramm. Eng. and Remote Sens.* 68, 821-829.

Figures

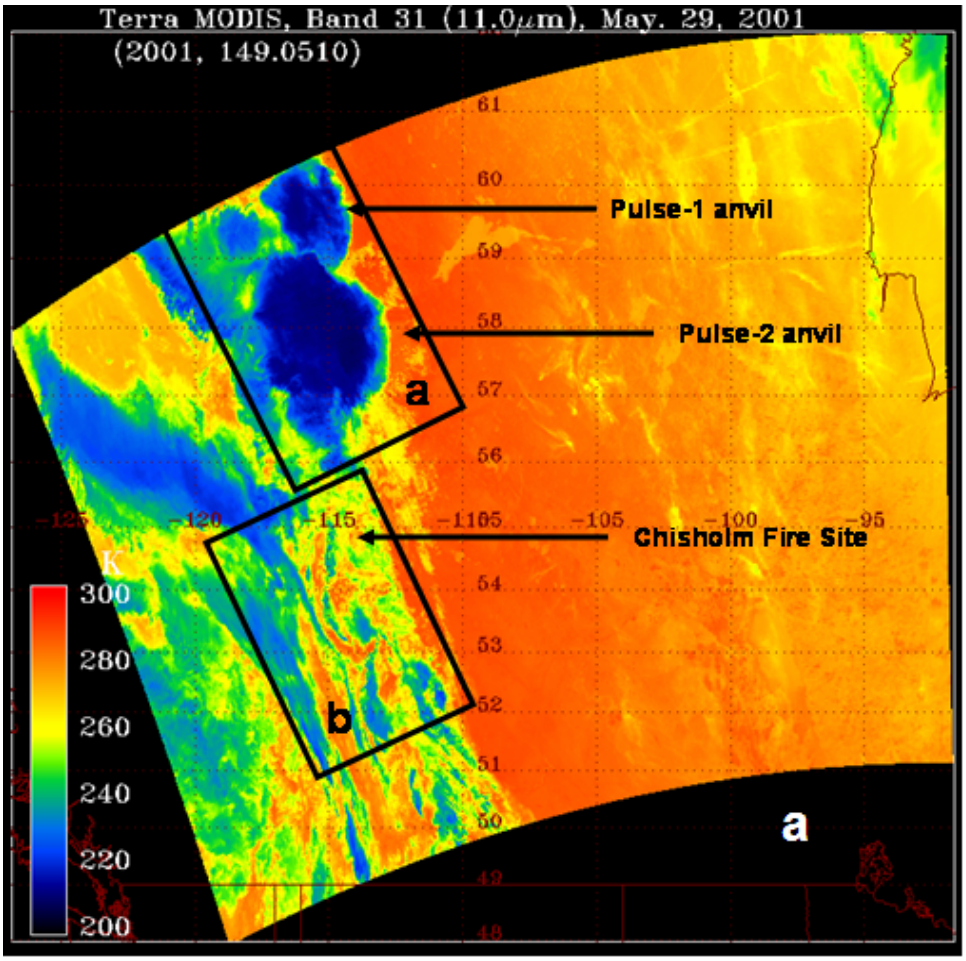
Terra MODIS, Band 31 (11.0μm), May. 29, 2001
(2001, 149.0510)
Pulse-1 anvil
Pulse-2 anvil
Chisholm Fire Site
a
b
a
K
300
280
260
240
220
200

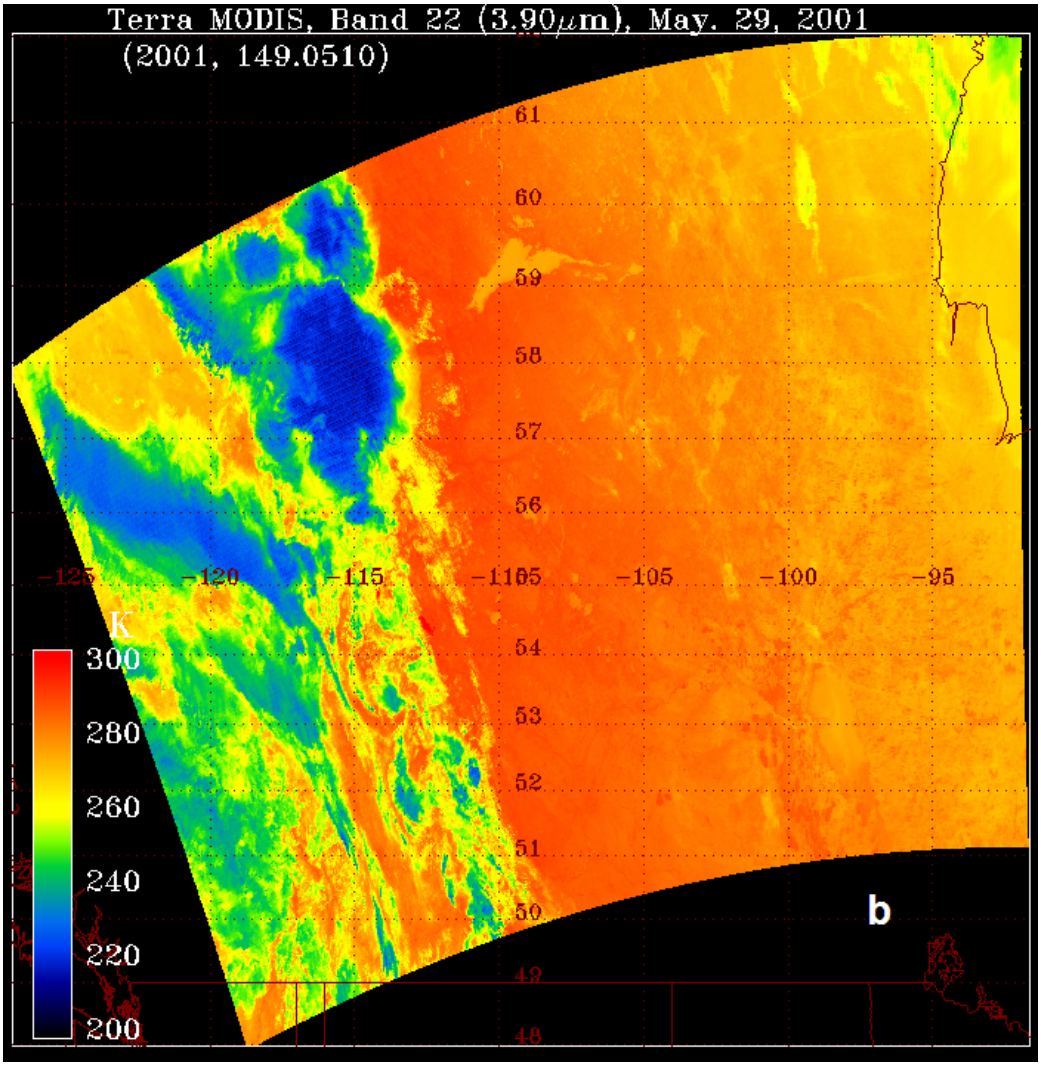
Terra MODIS, Band 22 (3.90μm), May. 29, 2001
(2001, 149.0510)
61
60
59
58
57
56
-125
-120
-115
-110
-105
-100
-95
K
300
280
260
240
220
200
54
53
52
51
50
49
48
b

1

2

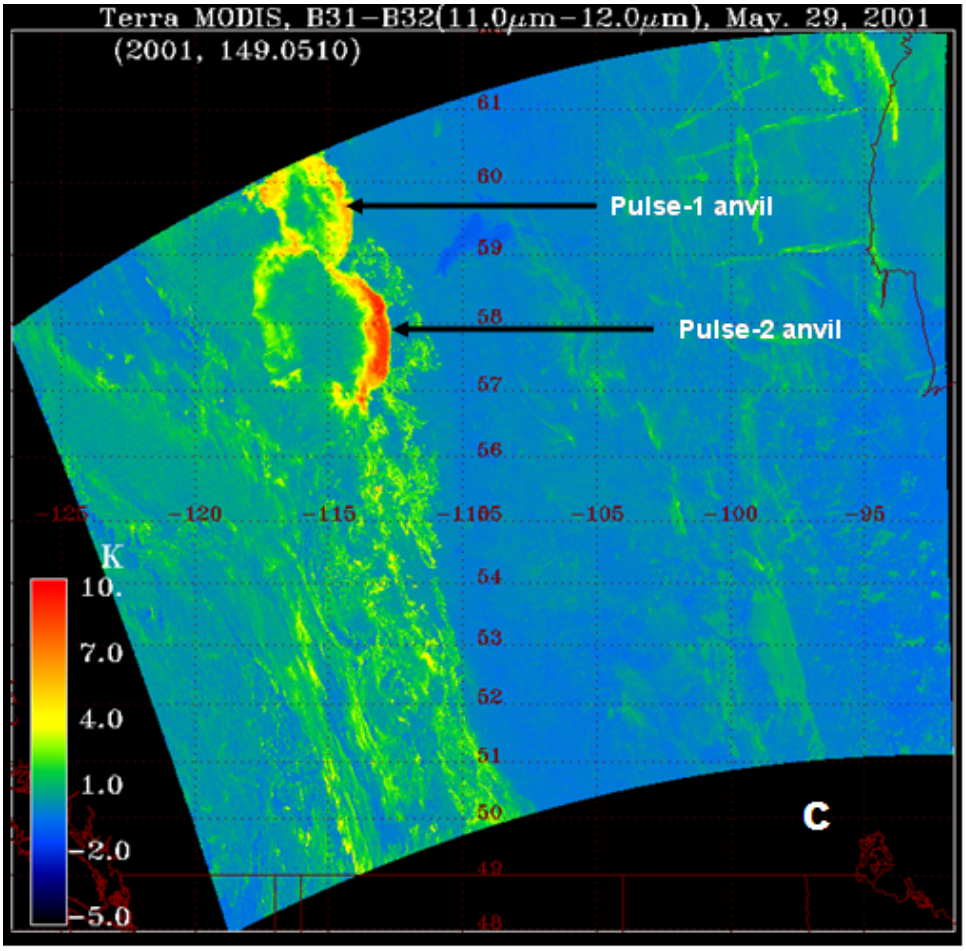

Figure 1. Terra MODIS IR nighttime brightness temperature (BT) imagery at 0510 UTC 29 May 2001. (a) 11 μm BT. (b) 3.9 μm BT. (c) 11-12 μm brightness temperature difference (BTD). Arrows identify features discussed in the text. Boxes on (a) show scenes for which a BTD analysis is performed (Figure 2).

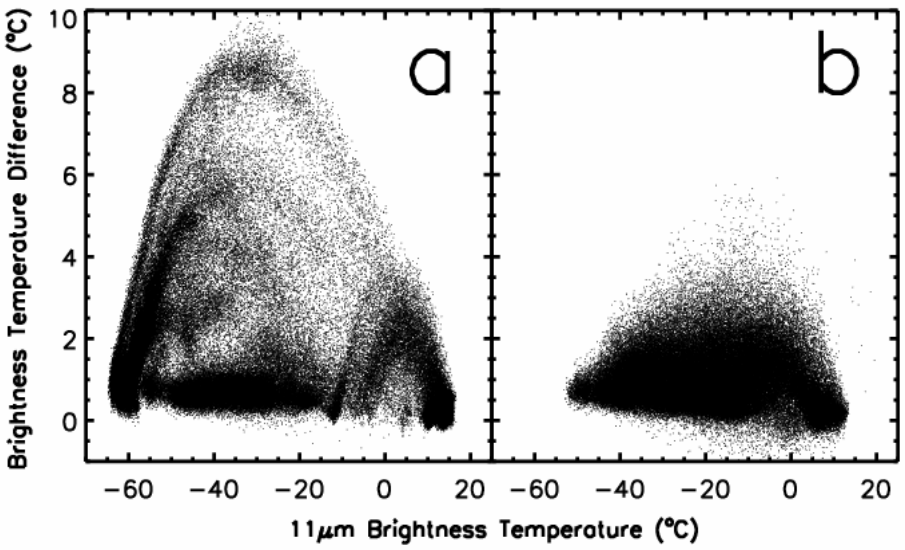

Figure 2. MODIS split-window BTD analysis, 0510 29 May 2001. Independent variable is 11μm BT (°C); dependent variable is 11-12μm BTD. (a) scene focused on Chisholm pyroCb blowoff; includes some meteorological cloud and clear sky. (b) scene with exclusively meteorological cloud that includes many with cold (i.e. deep, higher than the homogeneous freezing level) cloud tops.

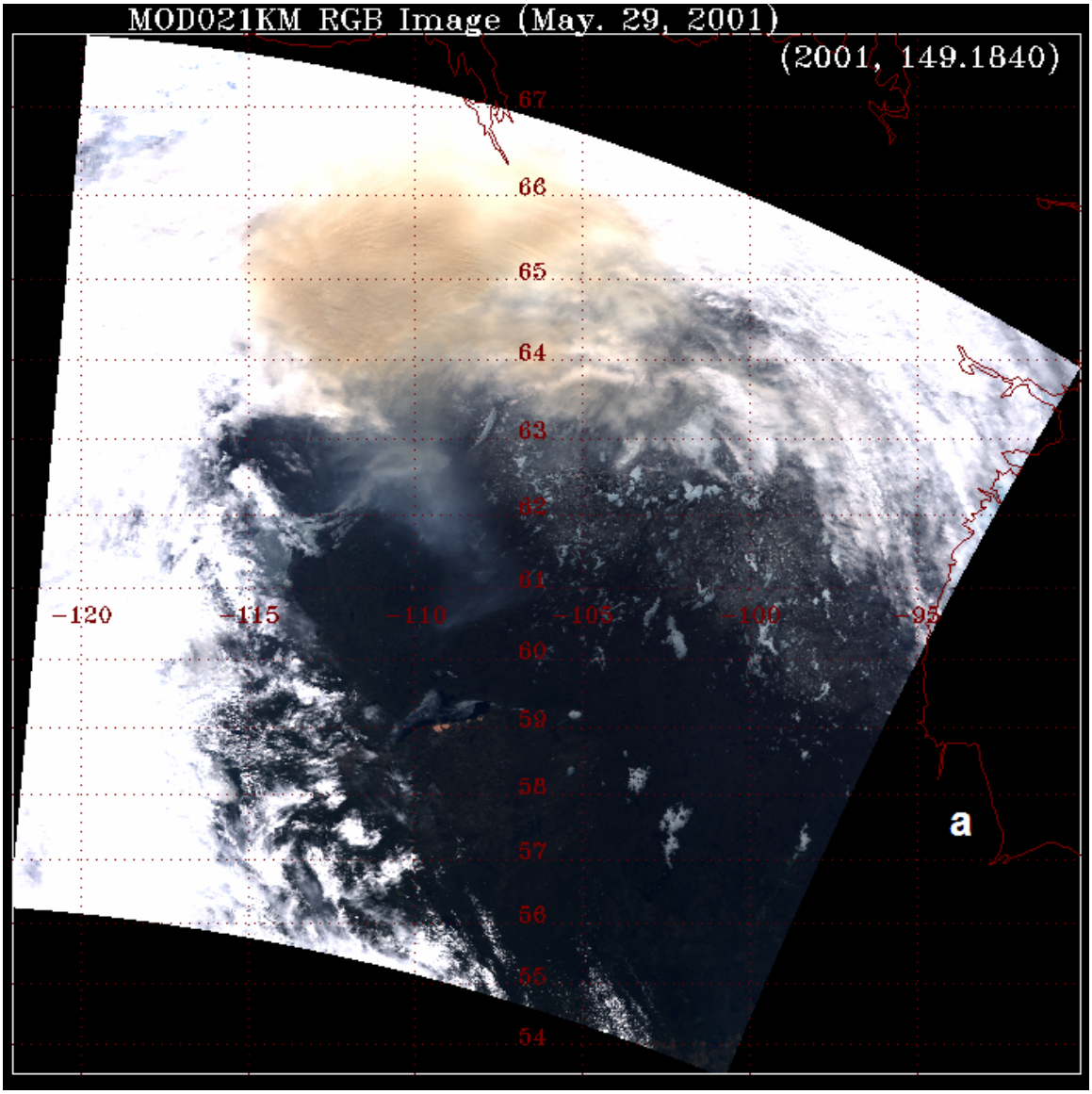
MOD021KM RGB Image (May. 29, 2001)
(2001, 149.1840)
67
66
65
64
63
62
61
60
59
58
57
56
55
54
−120
−115
−110
−105
−100
−95
a

1

2

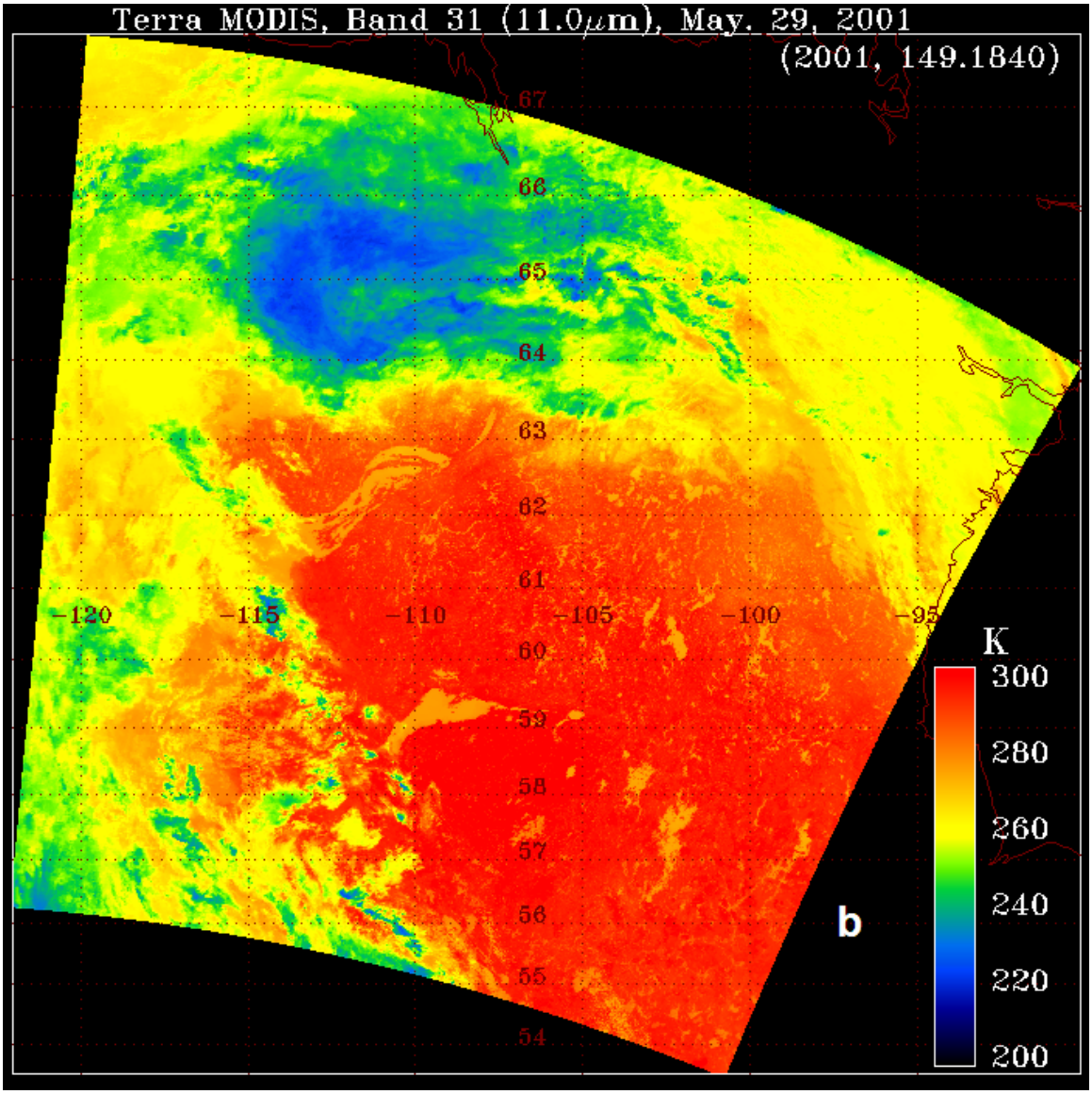
Terra MODIS, Band 31 (11.0μm), May. 29, 2001
(2001, 149.1840)
67
66
65
64
63
62
61
60
59
58
57
56
55
54
−120
−115
−110
−105
−100
−95
K
300
280
260
240
220
200
b

1

2

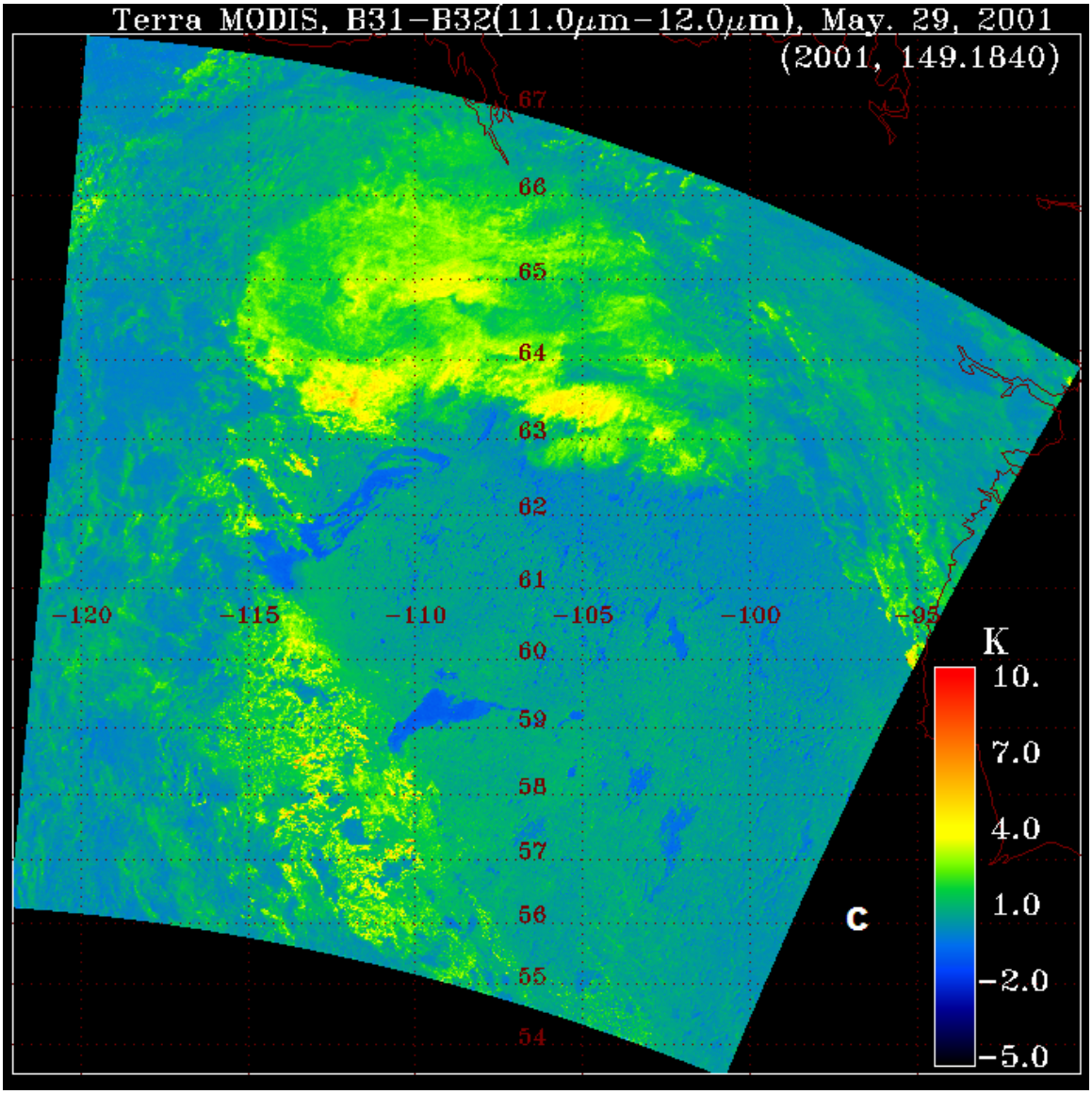
Terra MODIS, B31−B32(11.0μm−12.0μm), May. 29, 2001
(2001, 149.1840)
67
66
65
64
63
62
61
60
59
58
57
56
55
54
−120
−115
−110
−105
−100
−95
K
10.
7.0
4.0
1.0
−2.0
−5.0
c

1

2

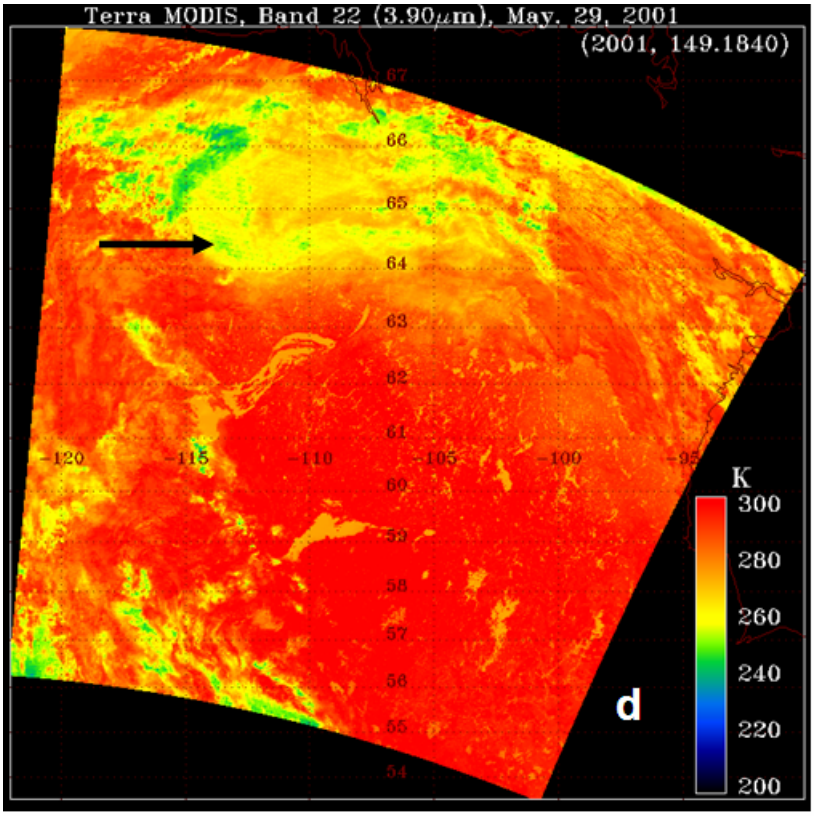

1

2 **Figure 3**. MODIS daytime true-color and infrared imagery at 1840 UTC 29 May 2001.

3 (a) stretched true color. (b) 11μm BT. (c) 11-12μm BTD. (d) 3.9μm BT.

4

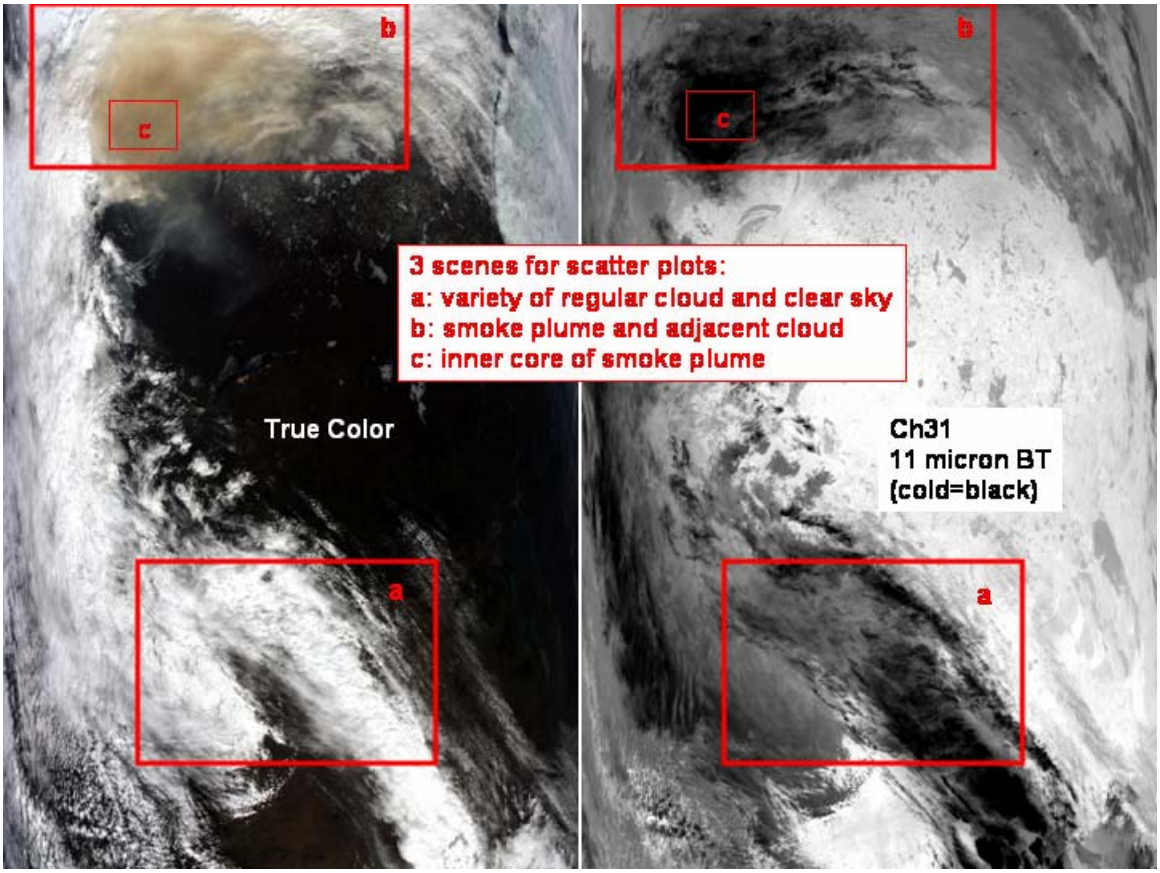

Figure 4. MODIS true color and 11μm BT at 1840 UTC 29 May, with boxes discriminating 3 scenes for split-window BTD analysis. Scene (a) contains only meteorological cloud. Scene (b) contains the smoke plume and surrounding meteorological cloud. Scene (c) is restricted to the smoky core of the plume.

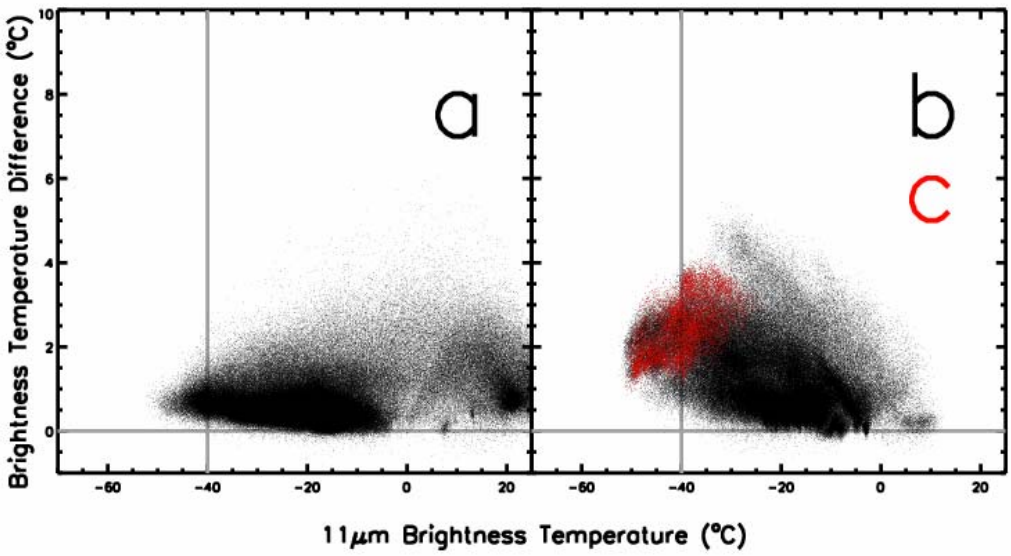

1

2

3 **Figure 5**. BTD analysis for 1840 UTC 29 May. Abscissa and ordinate ranges are

4 identical to 0510 UTC analysis in Figure 2. Panel (a) is for scene a of Figure 4. Panel (b)

5 has both scenes b (black dots) and c (red dots).

6

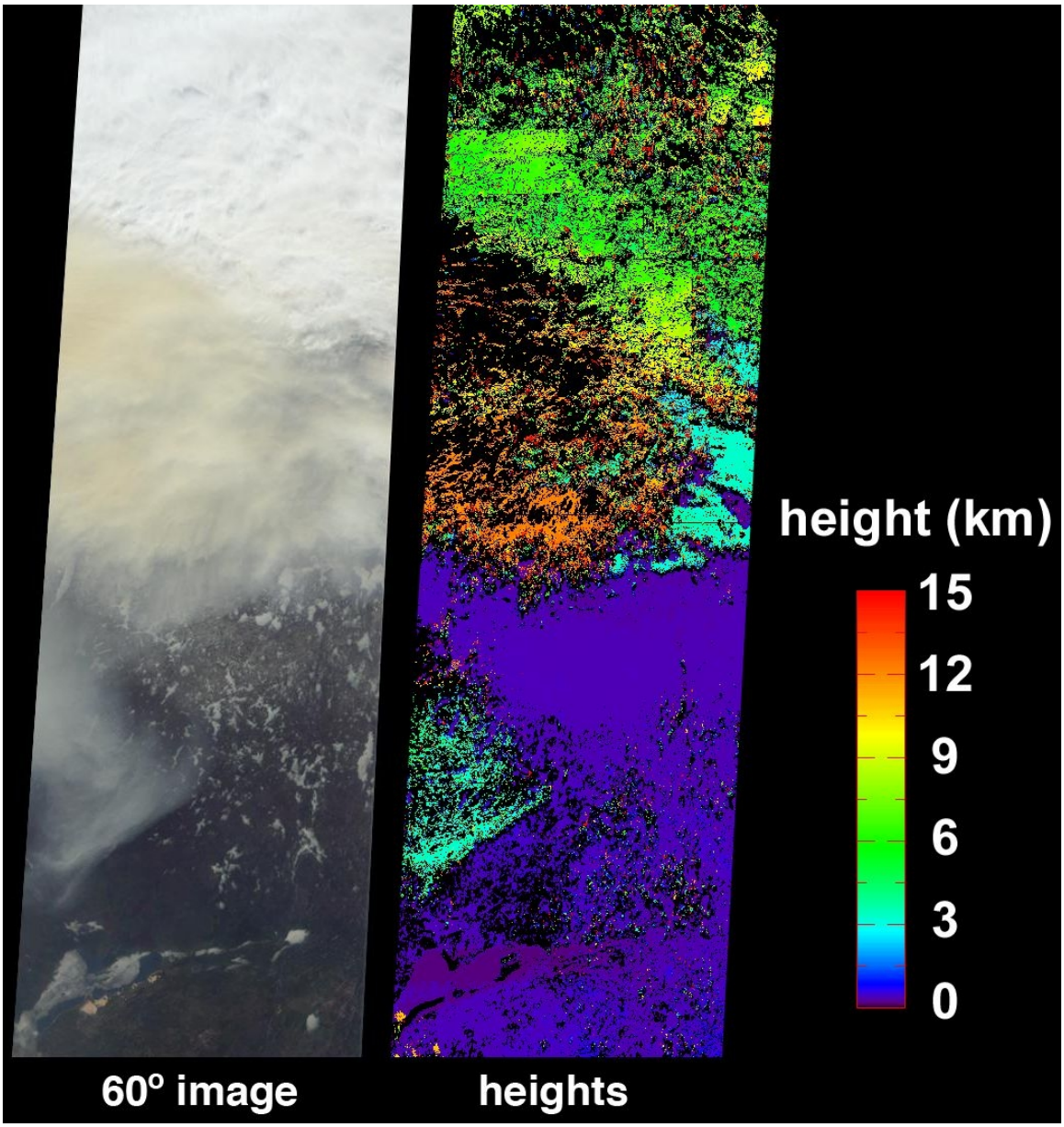

Figure 6. MISR true-color and stereo heights of 1840 UTC 29 May 2001 Chisholm plume and meteorological cloud to the northeast. The true-color image is from the 60° forward camera. The stereo heights are a special retrieval using MISR's 46° and 60° forward-pointing cameras.

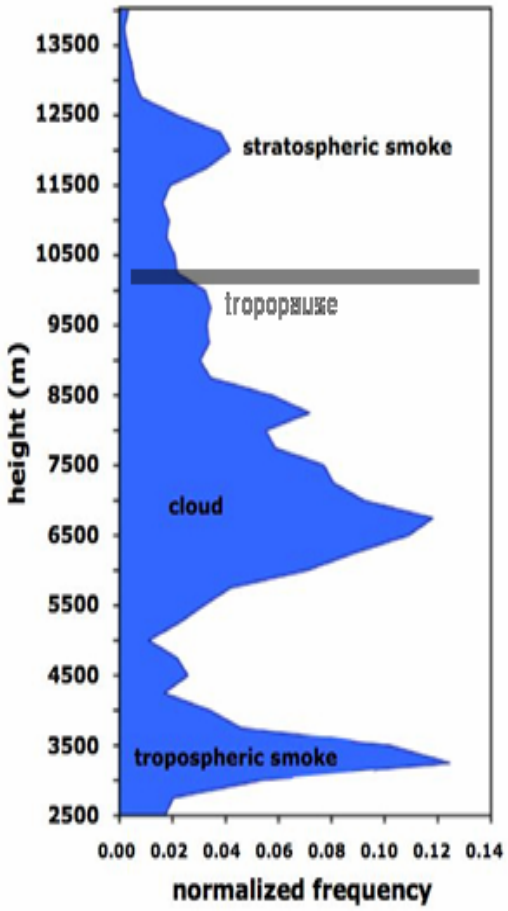

Figure 7. "Profile" of MISR stereo heights. This is a stereo-height frequency distribution. Local maxima and the cloud/plume subscenes which they represent are labeled. Tropopause height from Fort Smith (60°N, 110°W) radiosonde is marked by the gray bar.

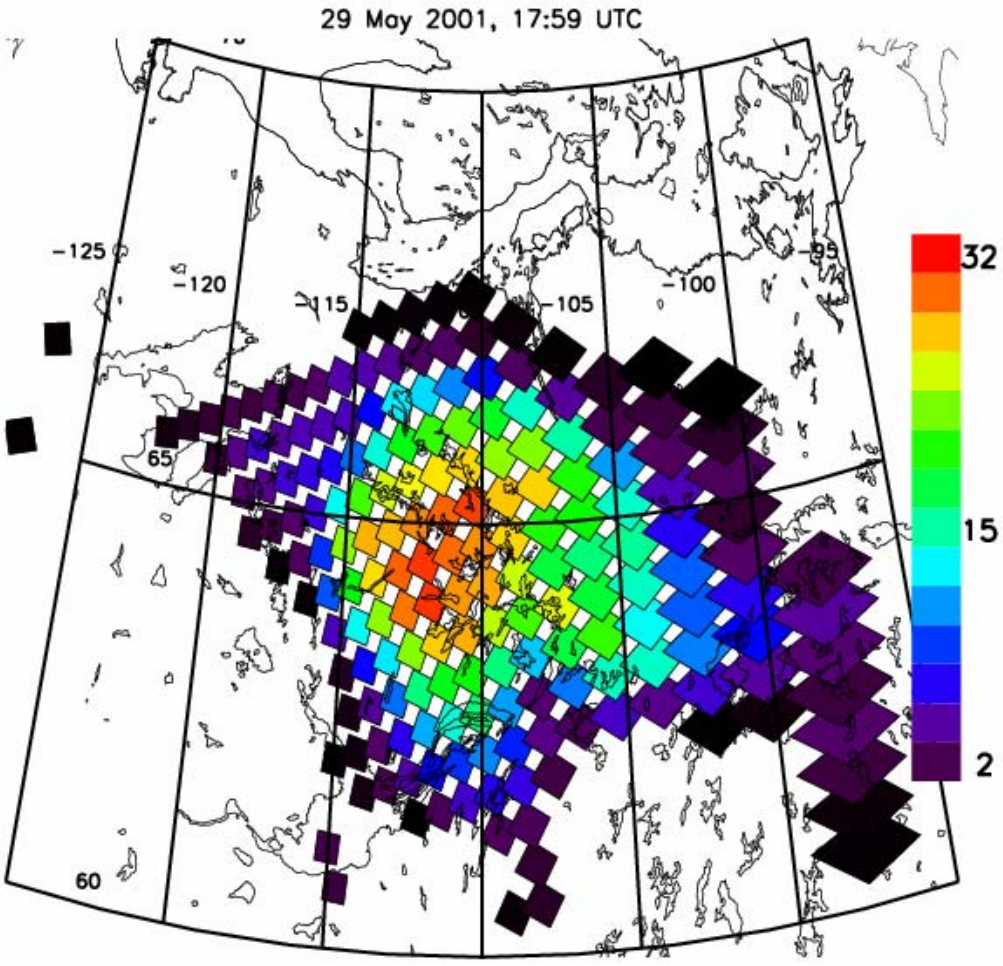

1
2

Figure 8. Earth-Probe TOMS level 2 aerosol index at ~18 UTC 29 May 2001.

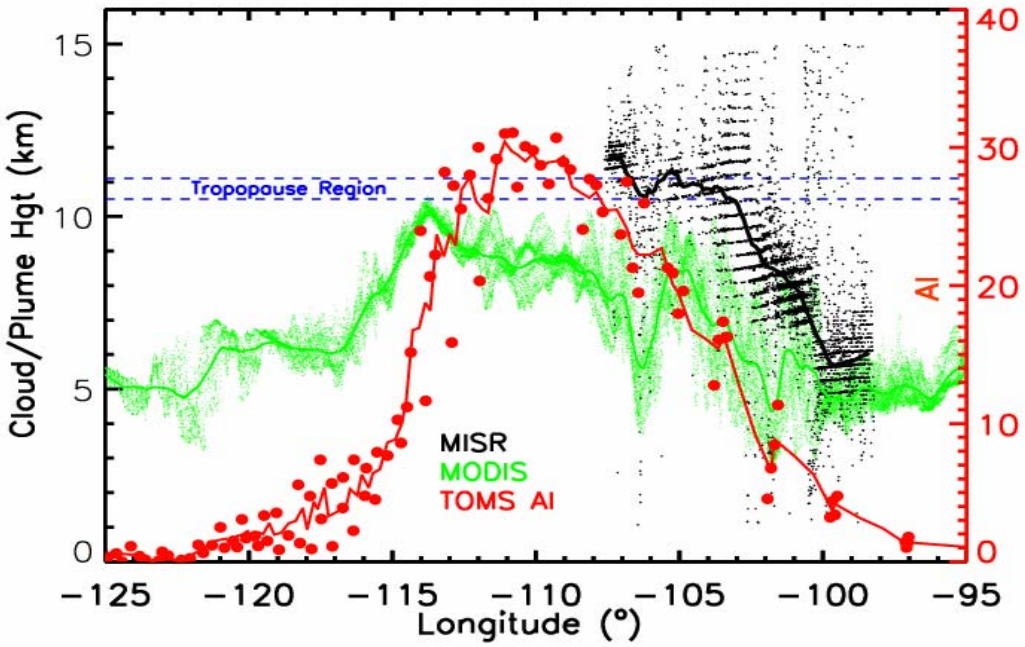

Figure 9. Analysis of MISR stereo heights, TOMS AI, and MODIS IR-inferred cloud tops along the 65°N parallel. All pixels within 2° of 65°N are shown. For details of MODIS BT-to-cloud-top altitude determination, see text. Lines through each data item are from boxcar smoothing. For tropopause-region determination, see text.

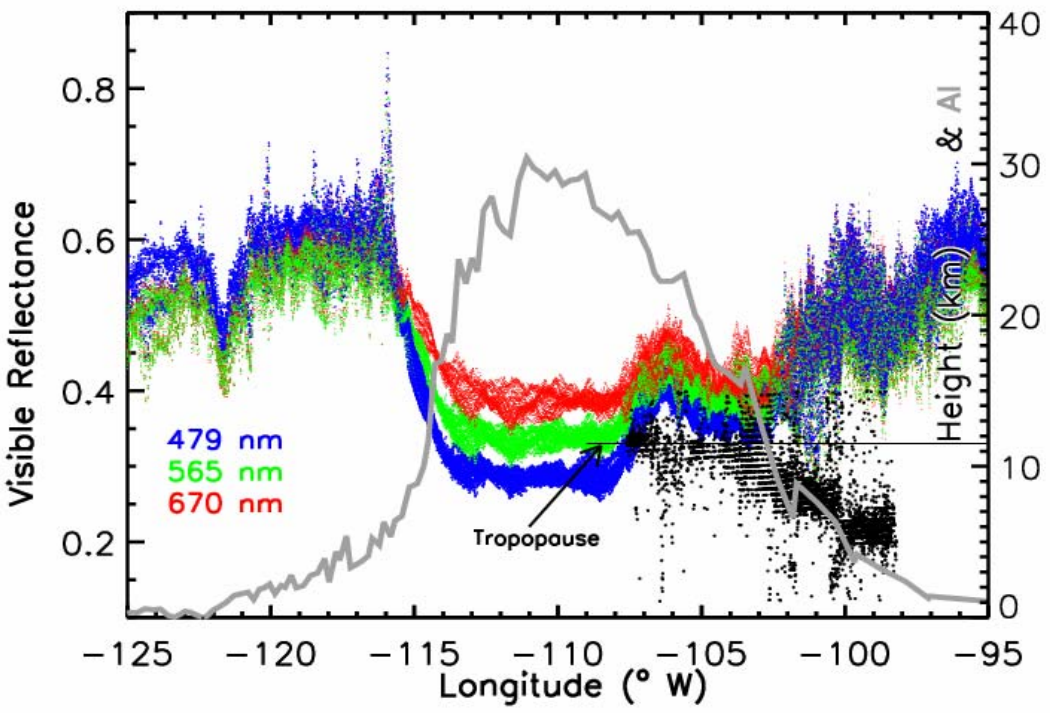

1

2

3 **Figure 10**. Analysis like in Figure 9, but with MODIS true-color-channel reflectances

4 instead of cloud-top. Each color channel is appropriately color coded.

5

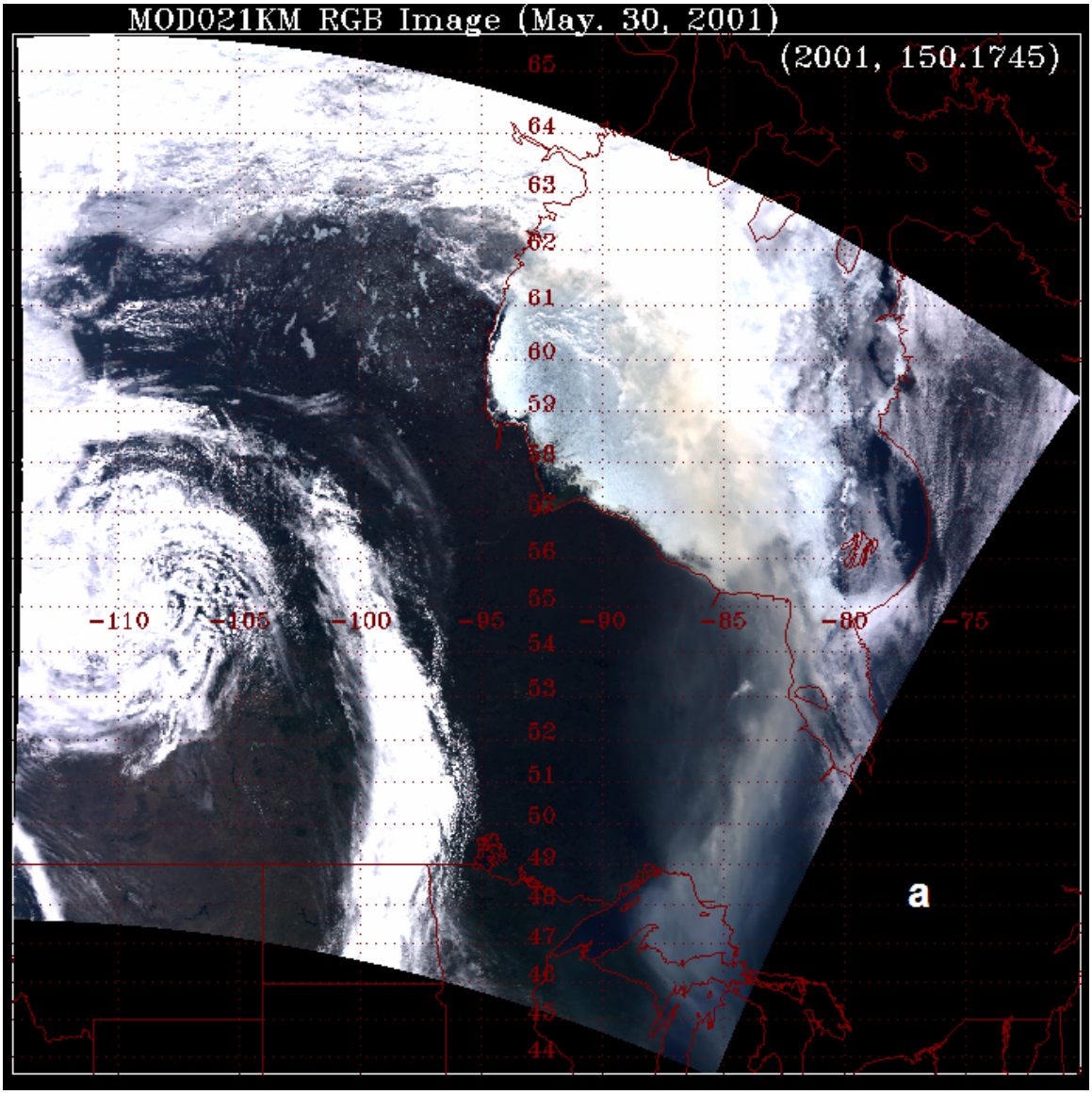
MOD021KM RGB Image (May. 30, 2001)
(2001, 150.1745)
65
64
63
62
61
60
59
58
57
56
55
54
53
52
51
50
49
48
47
46
45
44
-110
-105
-100
-95
-90
-85
-80
-75
a

1

2

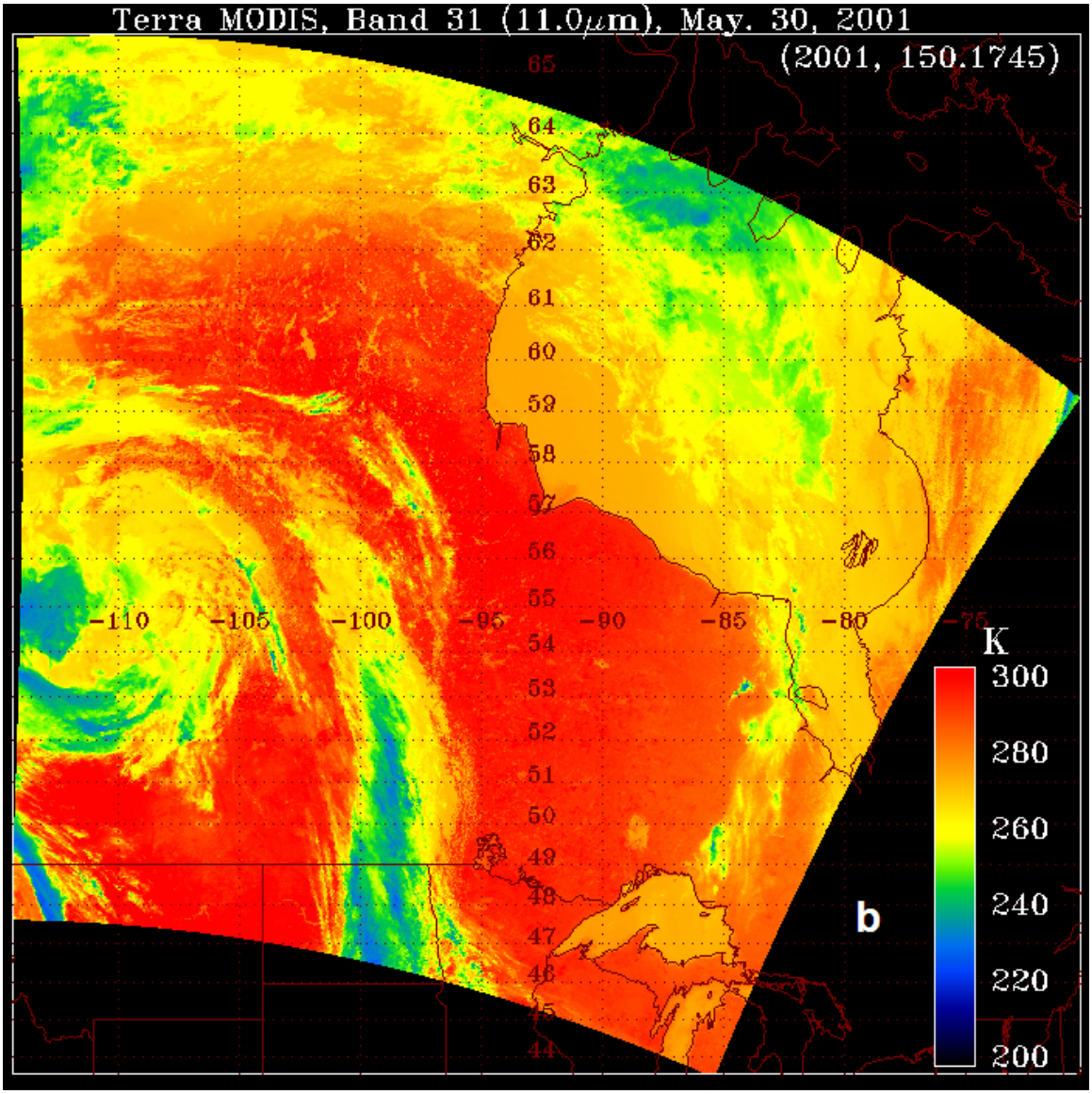

Figure 11. MODIS stretched true color (a) and 11μm BT (b) images for 1745 UTC 30 May 2001.

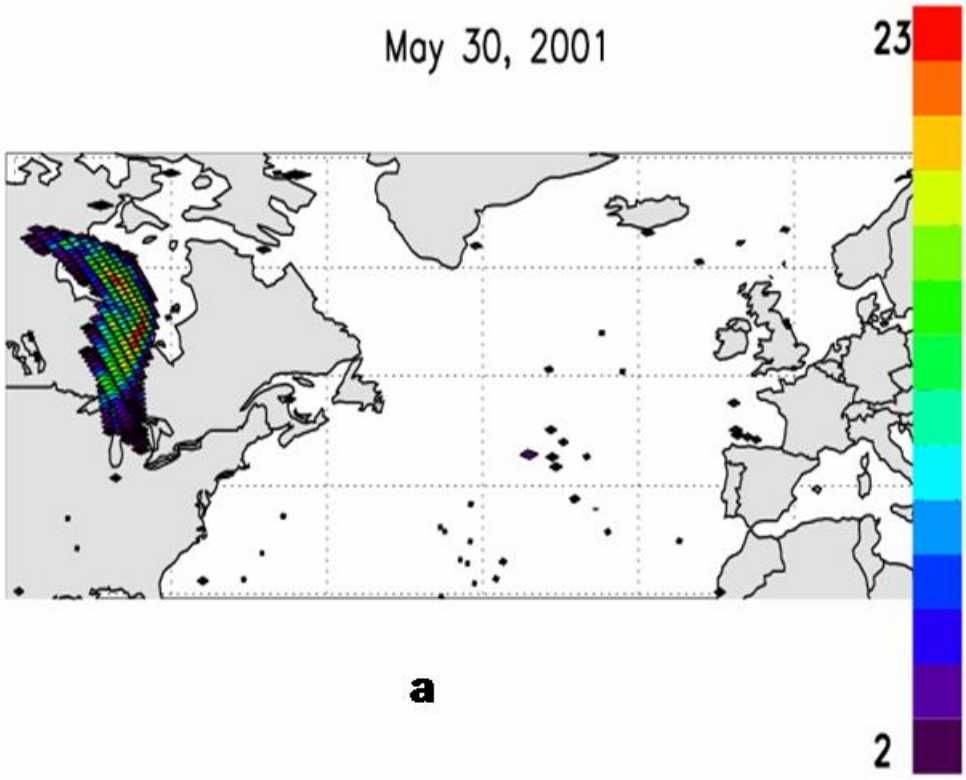

1

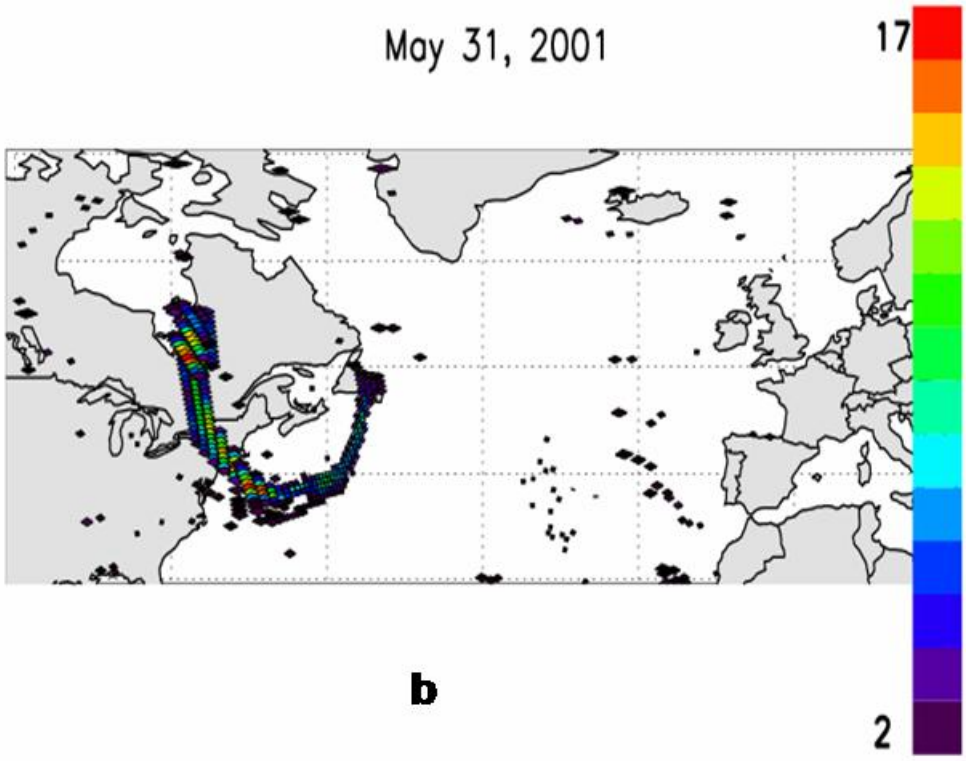

1

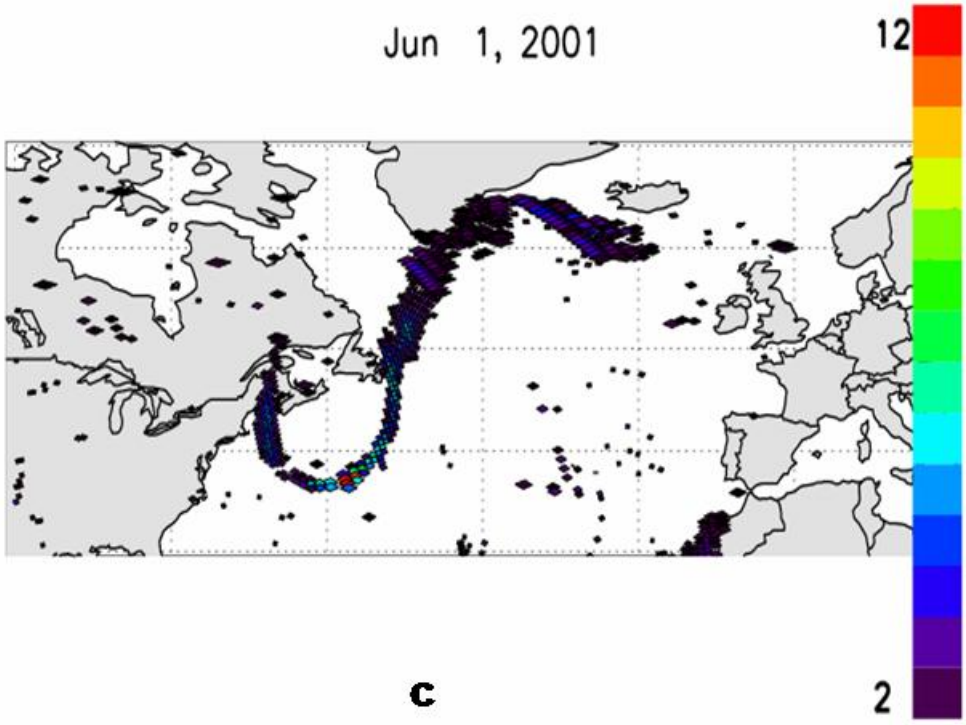

1

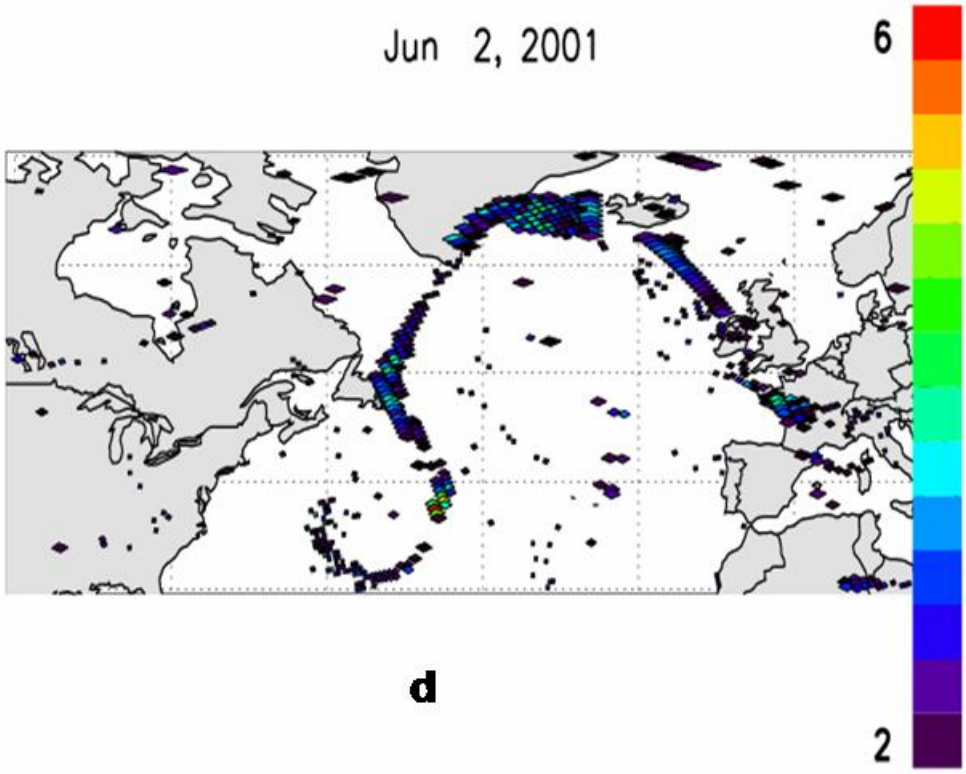

1

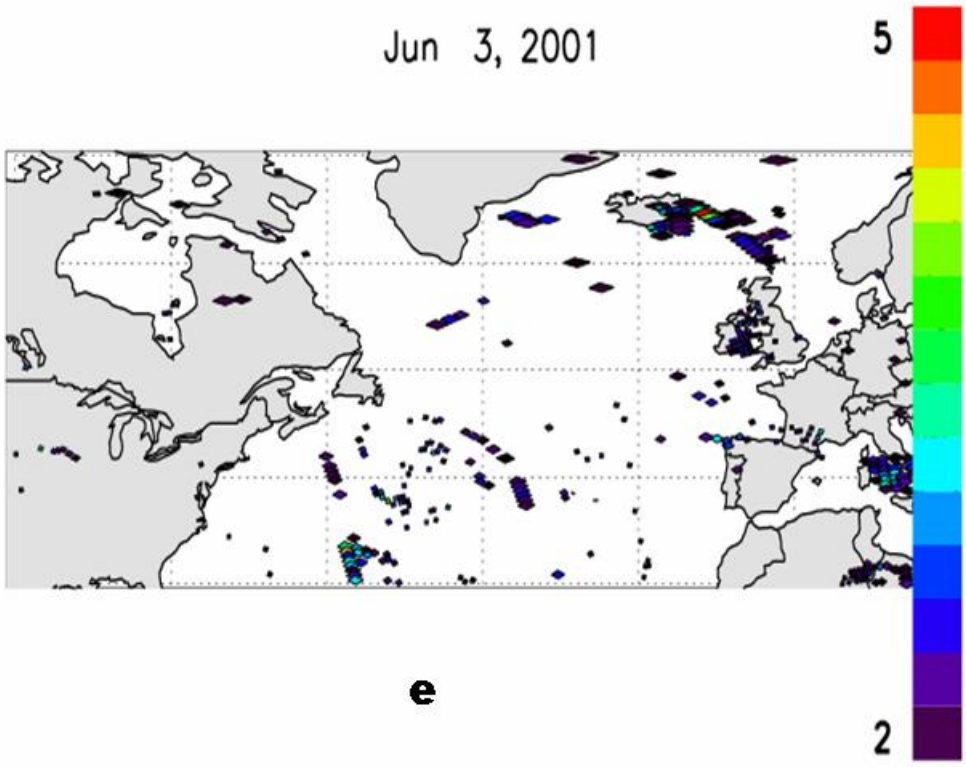

1

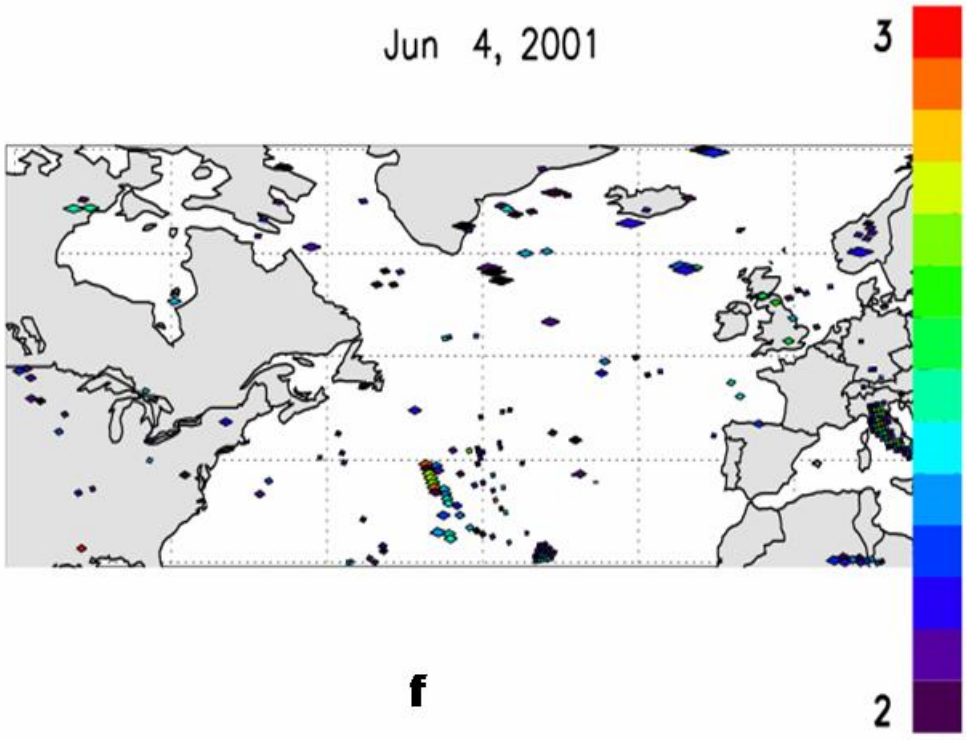

1

2 **Figure 12**. TOMS level 2 AI for 30 May – 4 June 2001 (a-f). Pixel rainbow color scaling
3 goes from AI=2 to the daily maximum.